Power Electronic Systems
Laboratory

IEEE Transactions on Power Electronics, Vol. 36, No. 3, pp. 2548-2563, March 2021

Transient Calorimetric Measurement of Ferrite Core Losses up to 50MHz

P. Papamanolis,
T. Guillod,
F. Krismer,
J. W. Kolar

Eidgenössische Technische Hochschule Zürich
Swiss Federal Institute of Technology Zurich

Transient Calorimetric Measurement of Ferrite Core Losses up to 50 MHz

Panteleimon Papamanolis, Thomas Guillod, Florian Krismer, and Johann W. Kolar

Power Electronic Systems Laboratory (PES)
ETH Zurich, Physikstrasse 3
8092 Zurich, Switzerland
Email: papamanolis@lem.ee.ethz.ch

***Abstract*—An accurate and fast transient calorimetric ferrite core-loss measurement method is proposed in this paper. In contrast to electrical measurements, the accuracy of the calorimetric approach is largely independent of the magnetic excitation and operating frequency. However, accurate values of the thermal capacitance and the temperature of the Core Under Test (CUT) are required. Accurate measurement of the specific heat capacity of the core material can be achieved with a Differential Scanning Calorimeter (DSC) or by using the CUT as a DC electric conductor and measuring its thermal response for known Joule heating. Accurate temperature measurements can be realized with NTC temperature sensors. A thorough uncertainty analysis of the presented method is conducted by identifying the impact of each source of uncertainty in the course of a sensitivity analysis. For the considered reference case (R 22.1/13.7/7.9 toroidal core with N49 ferrite material by EPCOS-TDK - 500 kHz/100 mT) the method achieves a total uncertainty with a worst-case value of less than 12 % or, in case of a more realistic approach considering a Gaussian distribution of each source of uncertainty, a mean value of -4.3 % with a 95 % confidence interval of ±3.2 %. The results are verified by means of FEM simulations and experiments. Furthermore, a step-by-step description of the workflow for preparing and conducting the experiments is provided. The proposed method is tested experimentally and compared to a state-of-the-art electrical loss measurement method for MnZn N87 and N49 ferrite cores of EPCOS-TDK. In addition, it is used to measure the loss-map of the NiZn ferrite material 67 from Fair-Rite for very high frequencies up to 50 MHz, which enables the computation of the material's Steinmetz parameters.**

***Keywords*—Magnetic losses, loss measurement, ferrites, MnZn, NiZn, high frequencies, transient calorimetry, specific heat capacity, differential scanning calorimeter, DSC, FEM.**

I. Introduction

Latest GaN power semiconductors enable very high switching frequencies and efficiencies of power electronics converters. In order to fully utilize the potential of available technologies, the design of power electronic converters is based on multi-objective optimization, e.g., with respect to power density and efficiency, which, however, relies on accurate component models. However, the power semiconductors' switching losses and the magnetic components' core losses are known to be subject to high uncertainties. Accordingly, the accurate knowledge of the switching losses and the losses of magnetic components of the converter circuits up to the MHz range is of great interest. This is particularly challenging for the core losses, whose behavior is highly non-linear, e.g., with respect to frequency, temperature, AC flux density, and DC premagnetization. Such non-linear dependencies apply especially to ferrite materials, MnZn (20 kHz to 2 MHz) and/or NiZn (1 MHz to 50 MHz), which are best suited for high frequency operation.

The main existing core loss measurement methods can be classified into electrical and calorimetric approaches [1]. Common problems to electrical methods, e.g., poor power factor and limitation to sinusoidal excitation have been resolved in [2]–[9]. State-of-the-art electrical methods feature partial cancellation of the phase-discrepancy error using an air-core inductor or a high-Q capacitor, in order to ensure adequate accuracy also at high frequencies, i.e., in the MHz range [10], [11]. However, the requirement of precise pre-calibration, elaborate post-processing, and difficulties arising from dealing with parasitics remain as drawbacks.

A steady-state calorimetric measurement [12]–[14] presents an alternative approach. However, the time needed for every single measurement is very long, i.e., typically in the range of several tens of minutes, and the realization of such setup is a challenging task. A transient calorimetric measurement method of core losses would drastically reduce the measurement time as shown for power semiconductors in [15]. An adaptation of this method to magnetic components is proposed in [16]. However, the presented approach requires a complex setup with an additional "calorimeter block", which refers to a block of known mass and thermal heat capacity (e.g., copper). The magnetic component is thermally well connected to the block and the total losses (both coil and core losses) can be measured through the rate of rise of the temperature of the copper block. In addition to its complexity, the proposed method requires calibration measurements in order to identify the heat flux leaking through the insulation. A simpler method to identify the core losses in a transient calorimetric approach is introduced in [17], which mainly relies on the correlation between the core losses and the rate of change of the core temperature. However, the method has only been used to measure the relative increase of the core losses, in presence of different levels of DC premagnetization, and has not been evaluated with regard to absolute core loss measurements. Finally, in [18] an effort to measure the absolute core losses using a transient calorimetric approach is presented, however, the work does not provide a detailed

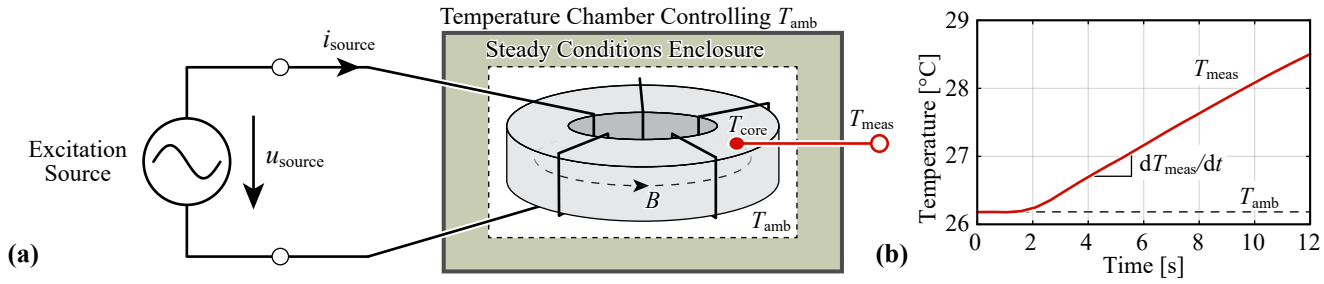

Fig. 1. (a) Proposed transient calorimetric core loss measurement setup: Core Under Test (CUT) with temperature sensor, enclosure (to achieve steady ambient conditions), and temperature chamber. (b) Example of the acquired increase of the core temperature over time.

investigation of the uncertainties of the method (e.g., with respect to the specific heat capacity of the measured core material, where a constant value is considered) as well as further verification (e.g., experimental results).

In this paper, the method presented in [18] is further developed, and a detailed investigation of the measurement uncertainties is introduced. The method is found to achieve a total measurement uncertainty of less than 20 % in a wide range of core losses, e.g., 40 mW < P_{core} < 8 W. Accordingly, it is well suited for core loss measurements, in particular at operating points where electrical measurement methods are subject to high uncertainties, e.g., at very high frequencies. The operating principle of the proposed measurement method is detailed in **Section II**. **Section III** presents an analysis of the implications of the individual measurement inaccuracies on the measured core losses, a derivation of the total measurement uncertainty for given specifications, and an investigation of the useful loss-range of the method. The results of the analysis are verified by means of FEM simulations in **Section IV**. Finally, **Section V** provides a step-by-step description of the workflow for preparing and conducting the experiments. Furthermore, Section V presents the experimental results for the investigated transient calorimetric method for two MnZn ferrite materials and a NiZn ferrite material and for frequencies up to 750 kHz and 50 MHz, respectively.

II. Experimental Setup and Operating Principle

Fig. 1 depicts the setup that consists of the Core Under Test (CUT) and an enclosure that ensures steady ambient conditions (e.g., homogeneous temperature, absence of air-flow) and improves the accuracy of the measurement due to the prevention of forced cooling (cf. Sec. III-B). If the measurement needs to be conducted at an ambient temperature, T_{amb}, that is different than the nominal ambient temperature, a reference temperature chamber, preferably an oven, can be used for that purpose. During the measurements of the presented work, a laboratory oven that uses forced air circulation and achieves a highly stable ambient temperature was employed. Small fluctuations around the reference temperature are of low importance, due to the substantially different time constants between the fluctuations of the temperature of the oven (multiple minutes) and the duration of a single experiment of the proposed method (tens of seconds). Finally, a high accuracy temperature sensor is attached to the core (cf. Fig. 1).

A. Fundamental measurement principle

For a given excitation and a negligible heat flux to the ambient, the temperature of the core increases according to

$$P_{core} = C_{th,core}\frac{dT_{core}}{dt} \approx C_{th,core}\frac{\Delta T_{meas}}{\Delta t}, \qquad (1)$$

where $C_{th,core}$ is the thermal capacitance of the core, T_{core} is the core temperature, and T_{meas} denominates the temperature reading.

According to (1), the correlation between the measured losses and the temperature only depends on the thermal capacitance of the core and not on the shape of the core or on the particular waveform of the flux density in the core. Compared to high-accuracy electric measurement procedures, time consuming steps that need to be conducted for each operating point, e.g., calibration of the setup and adaptation of the components for compensation, depending on the operating point [5]–[8], [10], [11], are avoided.

B. Equivalent thermal network

Fig. 2(a) depicts the considered equivalent thermal network of the experimental setup. The CUT is represented by the source of losses, P_{core}, and its thermal equivalent circuit elements, $R_{th,core}$ and $C_{th,core}$. The thermal resistance $R_{th,leak}$ models the heat leaking from the core to the ambient and to the coil through the mechanisms of thermal conduction, convection, and radiation. The setup employs two temperature sensors, i.e., the Negative Temperature Coefficient (NTC) thermistor,[1] considered with $R_{th,NTC}$ and $C_{th,NTC}$ in Fig. 2(a), and an IR camera, which, however, is only used for the purpose of verification and is not required for the core loss measurements. A look-up table is used to convert the resistance of the NTC to the measured temperature, $T_{NTC,meas}$, and a Savitzky-Golay filter, i.e., a filter based on a moving Least Mean Square (LMS) algorithm [19], is applied to decrease the measurement noise for the

[1]From an evaluation of different temperature sensors, also including Resistance Temperature Detector (RTD), and thermocouple sensors, the NTC thermistor has been selected due to its high immunity against induced electrical noise and the comparably fast response.

final temperature, $T_{\mathrm{meas}}(t)$, without distorting the required information.

This network can be simplified based on the following, experimentally supported (cf. Section III), considerations.

- $R_{\mathrm{th,core}}$ is assumed to be negligible (≈ 0), due to the relatively high thermal conductivities of MnZn and NiZn ferrite core materials ($\lambda \geq 3.5\,\mathrm{W/mK}$, cf. Section III-G).
- The NTC thermistor is represented by a low-pass filter with a time constant of τ_{NTC}, since $C_{\mathrm{th,NTC}} \ll C_{\mathrm{th,core}}$ applies.
- $C_{\mathrm{th,core}}$ is assumed to be constant during the course of a single experiment.

Fig. 2(b) shows the resulting simplified equivalent circuit, which is used for the thermal analysis. During the heating phase ($t \in [t_{\mathrm{on}}, t_{\mathrm{off}}]$ in **Fig. 3**), temperature independent core losses are assumed and the core temperature increases,

$$T_{\mathrm{core}}(t) = T_{\mathrm{amb}} + P_{\mathrm{core}} R_{\mathrm{th,leak}} \left(1 - \mathrm{e}^{-\frac{t-t_{\mathrm{on}}}{\tau_{\mathrm{leak}}}}\right), \tag{2}$$

$$\tau_{\mathrm{leak}} = R_{\mathrm{th,leak}} C_{\mathrm{th,core}}. \tag{3}$$

During the cooling phase ($t > t_{\mathrm{off}}$ in Fig. 3), zero core losses apply and the core temperature converges to the ambient temperature,

$$T_{\mathrm{core}}(t) = T_{\mathrm{amb}} + (T_{\mathrm{max}} - T_{\mathrm{amb}})\, \mathrm{e}^{-\frac{t-t_{\mathrm{off}}}{\tau_{\mathrm{leak}}}}. \tag{4}$$

According to (2) and (3), the values of $R_{\mathrm{th,leak}}$ and $C_{\mathrm{th,core}}$ are required for the computation of the core losses. $C_{\mathrm{th,core}}$ depends on the mass of the core and its specific heat capacity, which is a material property that can be acquired in advance using the methods discussed in Section III-A (or could be specified by the core manufacturer). $R_{\mathrm{th,leak}}$ depends on various factors, including the CUT, the coil, and the ambient conditions, and is estimated after each modification of the experimental setup.

For the estimation of $R_{\mathrm{th,leak}}$, two dedicated temperature values of the cooling phase, i.e., $T_{\mathrm{meas}}(t_2)$ and $T_{\mathrm{meas}}(t_2 + \Delta t_2)$ with $t_2 > t_{\mathrm{off}}$, are required. The resulting equation for $R_{\mathrm{th,leak}}$ is

$$R_{\mathrm{th,leak,est}}(t_2, \Delta t_2) = -\frac{\Delta t_2}{C_{\mathrm{th,core}}} \left[\ln\left(\frac{T_{\mathrm{meas}}(t_2 + \Delta t_2) - T_{\mathrm{amb}}}{T_{\mathrm{meas}}(t_2) - T_{\mathrm{amb}}}\right)\right]^{-1}. \tag{5}$$

Finally, P_{core} is estimated using two dedicated temperature values of the waveform acquired during the heating phase, $T_{\mathrm{meas}}(t_1)$ and $T_{\mathrm{meas}}(t_1 + \Delta t_1)$, with $t_{\mathrm{on}} < t_1 < t_1 + \Delta t_1 < t_{\mathrm{off}}$,[2]

$$P_{\mathrm{core,est}}(t_1, \Delta t_1) = \frac{T_{\mathrm{meas}}(t_1 + \Delta t_1) - T_{\mathrm{meas}}(t_1)}{\left(\mathrm{e}^{-\frac{t_1 - t_{\mathrm{on}}}{\tau_{\mathrm{leak}}}} - \mathrm{e}^{-\frac{t_1 + \Delta t_1 - t_{\mathrm{on}}}{\tau_{\mathrm{leak}}}}\right) R_{\mathrm{th,leak}}}. \tag{6}$$

[2]In an alternative approach, LMS approximations could be used to identify P_{core} and $R_{\mathrm{th,leak}}$, by fitting (2) and (4), respectively. However, this is computationally more demanding and, due to the noise reduction achieved with the Savitzky-Golay filter [19], the difference between LMS approximation and the described two-points approach is found to be consistently below 1 %.

TABLE I
SPECIFICATIONS AND OPERATING CONDITIONS FOR THE REFERENCE EXPERIMENTAL SETUP.

Parameter	Value
Core material	N49 (EPCOS-TDK)
Core shape	R 22.1 x 13.7 x 7.9
Operat. point	500 kHz / 100 mT
$C_{\mathrm{th,core}}$	7.3 J/K
$R_{\mathrm{th,leak}}$	45 K/W
P_{core}	1.54 W
T_{amb}	26.2 °C

C. Validation of the thermal equivalent network

The reference setup specified in **Tab. I** serves for the purpose of validation and employs an R 22.1/13.7/7.9 toroidal core (N49 by EPCOS-TDK) with a coil made of 10 turns of high-frequency litz wire ($180 \times 71\,\mu\mathrm{m}$). The CUT is subject to a sinusoidal excitation with a peak flux density of 100 mT at a frequency of 500 kHz, which leads to reasonable core losses of 1.54 W (cf. Section V-A1 for further details regarding the selection of a suitable CUT).

Figure 3 presents the core temperature measured with an NTC thermistor (Littelfuse, PS104J2 [20]) and an IR camera (FLIR, A655sc [21], 30 frames/sec), for the same excitation. In addition, the temperatures $T_{\mathrm{core,sim}}$ and $T_{\mathrm{NTC,sim}}$ are depicted, as extracted from a simulation of the circuit of Fig. 2. For the implementation of the simulation circuit the values of $C_{\mathrm{th,core}}$, $R_{\mathrm{th,leak}}$, and τ_{NTC} need to be known. In this regard, $C_{\mathrm{th,core}}$ is determined in advance (cf. Section III-A) and $R_{\mathrm{th,leak}}$ is estimated with (5) during the cooling phase of the measurement. The time constant of the NTC, $\tau_{\mathrm{NTC}} = 5.5\,\mathrm{s}$, is determined such that the difference between simulated and measured waveforms is minimal.

It is found that simulated and measured waveforms match for both measurements, i.e., core and NTC temperatures, with maximum deviations of 0.28 °C and 0.19 °C, respectively. Moreover, the resulting simulated model was further used and successfully reproduced the temperature waveforms of the same experimental setup for different induced core losses, ranging from 0.4 W to 4.5 W, which further verifies the applicability of the considered circuit.

III. MEASUREMENT ACCURACY

Typical sources of uncertainties in calorimetric measurement methods include the measurement accuracy of the employed equipment (e.g., temperature measurement device, DSC, time measurement device) and the impact of temperature on the measured quantities (e.g., generated core losses, specific heat capacity of the material, leaking heat during the experiment). In the course of an uncertainty analysis, the main sources of inaccuracies have been identified and are described in this Section:

- **Section III-A**: limited accuracy of the *thermal capacitance measurement*, $C_{\mathrm{th,core}}$.
- **Section III-B**: uncertainty of the estimated heat flux arising from the uncertainty of the employed *leakage flux model*, which considers heat transfer to the ambient

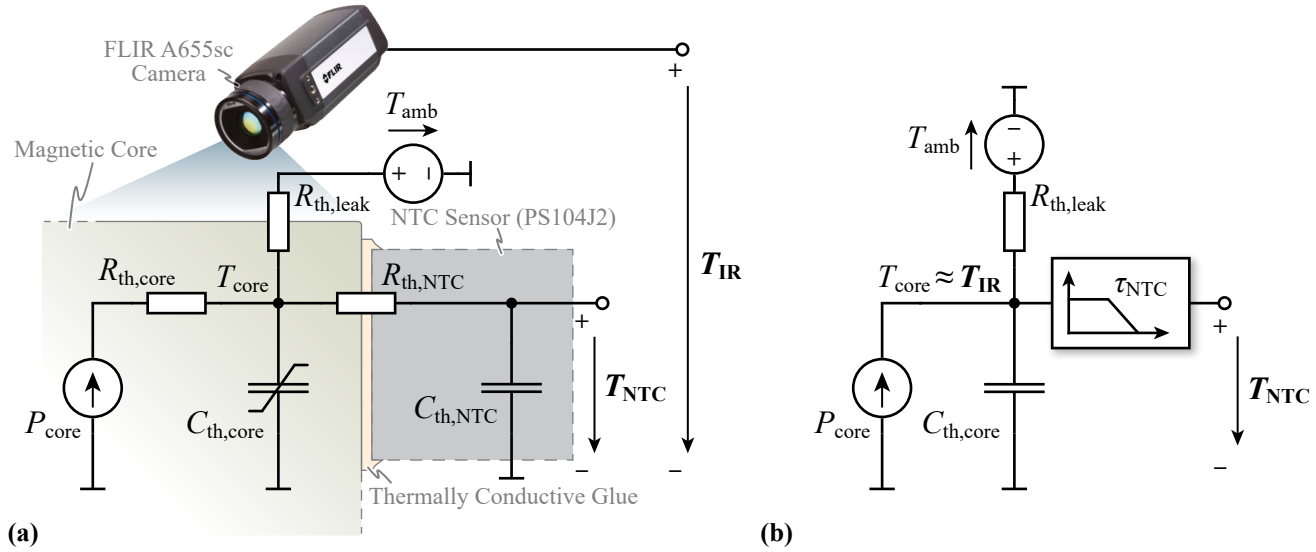

Fig. 2. (a) Equivalent circuit of the calorimetric experimental setup, including the Core Under Test (CUT), the attached NTC thermistor, and the high accuracy IR camera; (b) simplified version of the proposed equivalent circuit that is considered in this paper. The IR camera serves only for model verification and is not required for the measurement of the core losses.

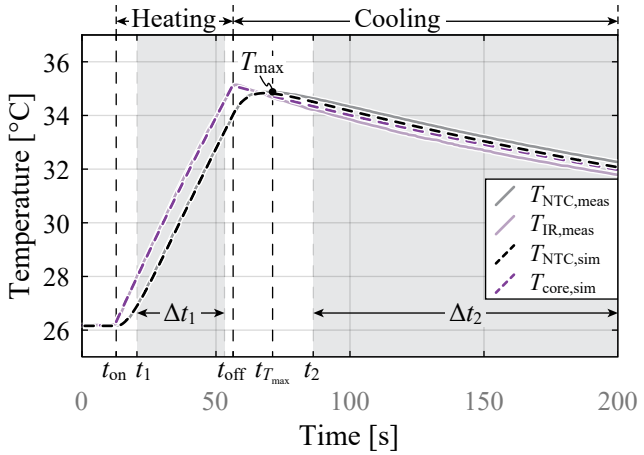

Fig. 3. Comparison of the results of a real measurement and a simulation of the thermal equivalent network of Fig. 2(b) using a toroidal ferrite core (R 22.1/13.7/7.9, N49) that is subject to a sinusoidal magnetic flux (100 mT, 500 kHz). The core temperature is measured with a NTC thermistor (Littelfuse PS104J2 [20]) and an IR camera (FLIR A655sc [21]) at 30 frames/sec. The component values of the simulated circuit are: $P_{core} = 1.54\,W$, $C_{th,core} = 7.3\,J/K$, $R_{th,leak} = 45\,K/W$, $\tau_{NTC} = 5.5\,s$.

and to the coil by means of conduction, convection, and radiation.

- **Sections III-C** and **III-D**: limited dynamic response and accuracy of the *temperature sensor*.
- **Section III-E**: limited *clock accuracy* of experiment time measurement.
- **Section III-F**: *temperature dependencies* of P_{core}, $R_{th,leak}$ and $C_{th,core}$.
- **Section III-G**: *temperature gradient in the core* due to non-homogeneous magnetic flux density and finite thermal conductivity of the core.
- **Section III-H**: implications of *copper losses*.

Tab. II lists the values of the inaccuracies, ξ, that have been determined for the reference setup specified in Tab. I and described in Section II-C. Tab. II further presents the expressions for the linearized sensitivities $\partial P_{core,est}/\partial\xi$ for the different inaccuracies, which can be used to estimate the boundaries of the uncertainties of the estimated core losses at each operating point (by way of example, the expression for $\partial P_{core,est}/\partial\delta_{C_{th,core}}$ is derived in Section III-A). **Tab. III** lists the values of the boundaries determined for the reference setup, using the simplified linearized expressions presented in Tab. II, and, for the purpose of verification, also the corresponding values obtained from a numerical evaluation of the non-linear differential equation of the investigated system. The total measurement uncertainty is finally determined according to Section III-I.

A. Uncertainty $\delta_{C_{th,core}}$ of core's thermal capacitance

Accurate knowledge of $C_{th,core}$ is of high importance, since it directly influences the calculated losses, cf. (1). Out of different measurement methods proposed in literature, the Differential Scanning Calorimetry (DSC) [22] features the best trade-off between complexity and accuracy. The basic operating principle of this method relies on the accurate measurement of the heat flow that is provided to a given sample, in order to achieve a defined increase of the sample's temperature, which enables the calculation of its differential specific heat capacity as a function of temperature. The employed DSC 2500, from TA Instruments [23], uses a sapphire sample as reference and provides a maximum measurement accuracy of 2 %. Nevertheless, due to the non-ideal discoid shape of the employed samples, the measurement accuracy was set to a conservative

$$\delta_{C_{th,core}} = \pm 3\,\%. \tag{7}$$

Fig. 4 depicts the specific heat capacities of three MnZn ferrite materials (N87, N97, and N49 of EPCOS-TDK) and of

TABLE II
UNCERTAIN PARAMETERS AND ERROR SOURCES.

	Parameter ξ	Description	Range	Linear Sensitivity, $\partial P_{\text{core,est}}/\partial\xi$
Considered	$\delta_{C_{\text{th,core}}}$	Uncert. of calc. core thermal capacitance	±3 %	$-P_{\text{core}}$
	$\delta_{R_{\text{th,leak}}}$	Uncert. of calc. leakage thermal resistance	±20 %	$P_{\text{core}}\left(\frac{t_1-t_{\text{on}}}{\tau_{\text{leak}}}+\frac{\Delta t_1}{2\tau_{\text{leak}}+\Delta t_1}\right)$
	$\epsilon_{T_{\text{meas}}}$	Differential temperature meas. uncertainty	±0.1 °C	$C_{\text{th,core}}/\Delta t_1$
	τ_{NTC}	Time constant of NTC sensor	[3 s, 5.5 s]	cf. (13)
	$\eta_{P_{\text{core}}}$	Change in core losses due to ΔT_{core}	−1 %/°C	$P_{\text{core}}^2\frac{\Delta t_1+2(t_1-t_{\text{on}})}{2C_{\text{th,core}}}$
Disregarded	$\epsilon_{t_{\text{meas}}}$	Time meas. error	$\pm 0.0001\times\Delta t_1$ s	$2P_{\text{core}}/\Delta t_1$
	$\eta_{C_{\text{th,core}}}$	Change in $C_{\text{th,core}}$ due to ΔT_{core}	0.1 %/°C	$-P_{\text{core}}^2\frac{\Delta t_1+2(t_1-t_{\text{on}})}{2C_{\text{th,core}}}$
	$\eta_{R_{\text{th,leak}}}$	Change in $R_{\text{th,leak}}$ due to ΔT_{core}	−1.2 %/°C	$P_{\text{core}}^2\frac{[\Delta t_1+2(t_1-t_{\text{on}})]^2}{2C_{\text{th,core}}(2\tau_{\text{leak}}+\Delta t)}$
	–	Additional heat from copper losses	–	–
	–	Temperature grad. in radial direction, due to non-homogeneous magnetic flux distribution	–	–

TABLE III
DEVIATIONS BETWEEN ACTUAL AND MEASURED CORE LOSSES, $\Delta P_{\text{LIN}} = \xi(\partial P_{\text{CORE,EST}}/\partial\xi)$, FOR THE REFERENCE SETUP AND THE OPERATING CONDITIONS LISTED IN TAB. I (CORE LOSSES ARE 1.54 W); VERIFICATION BASED ON NUMERICAL RESULTS OBTAINED FROM THE SYSTEM'S NON-LINEAR DIFFERENTIAL EQUATION.

ξ	ΔP_{lin} / mW (cf. Tab. II)	ΔP / mW (numerical eval. of diff. equ.)
$\delta_{C_{\text{th,core}}}$	±46.2	[−41.3, +43.7]
$\delta_{R_{\text{th,leak}}}$	±24.47	[−30.6, +20.8]
$\epsilon_{T_{\text{meas}}}$	±28.91	±31.3
τ_{NTC}	[−1.8, +12.4]	[−1.5, +12.4]
$\eta_{P_{\text{core}}}$	−86.3	−83.3
$\epsilon_{t_{\text{meas}}}$	$<\pm 1$	$<\pm 1$
$\eta_{C_{\text{th,core}}}$	−8.6	−7.8
$\eta_{R_{\text{th,leak}}}$	−8.1	−9.3

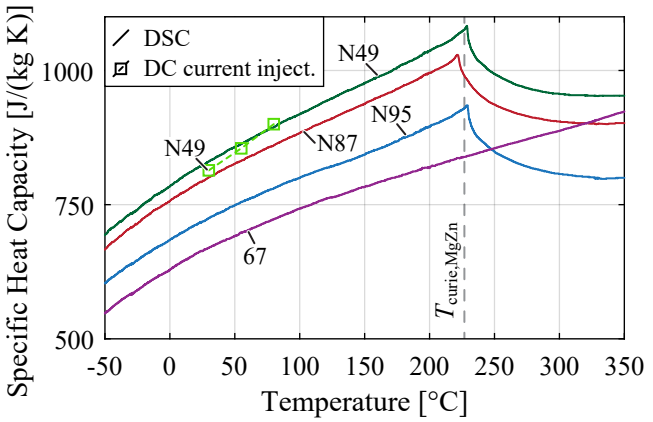

Fig. 4. Measured specific heat capacities of N87, N97 and N49 MnZn ferrite materials of EPCOS-TDK and 67 NiZn ferrite material of Fair-Rite using the Differential Scanning Calorimeter (DSC) 2500 of TA instruments. Additionally, for three different temperatures (30 °C, 55 °C, and 80 °C), the specific heat capacity of N49 is measured according to [28], where the ferrite conducts a DC current for generating a defined ohmic power loss in order to heat the core. With known DC losses, temperature rise, and core weight, the specific heat capacitance can be calculated.

one NiZn ferrite material (67 of FairRite). The specific heat capacities of all four materials are temperature dependent, and this is related to different microscopic processes on atomic and molecule level [24], [25]. The abrupt steps for MnZn materials at approximately 225 °C correspond to the Curie temperature [26], [27].

DSCs are commonly used in material science, however, they may be less accessible in power electronics. An alternative, more accessible, way for the measurement of $C_{\text{th,core}}$ is discussed in [28]: a sample of the considered material is used as a DC electric conductor ($\rho_{\text{MnZn}} \approx 10\,\Omega/\text{m}$ - strongly temperature dependent) and, by means of Joule heating, the thermal response of the core is used to determine $C_{\text{th,core}}$ using (1), cf. **Fig. 5**. For the sake of completeness, this method has also been applied to the N49 material at three different ambient temperatures, i.e., 30 °C, 55 °C, and 80 °C.

A rectangular block of MnZn N49 ferrite equal to $51.0\times 11.9\times 5.1\,\text{mm}^3$ / 14.806 gr is employed. This results in a block resistance, R_{block}, approximately equal to 9.72 kΩ (at 30 °C), 8.43 kΩ (at 55 °C), and 3.07 kΩ (at 80 °C). The block is placed inside an enclosure and the complete setup inside a temperature chamber (cf. Fig. 1). For each value of T_{amb}, a constant voltage is applied and the injected DC current is monitored. Due to the temperature dependent conductivity of ferrite material, the value of the injected losses is subject to minor change during the experiment. In such narrow temperature range the injected losses can be averaged. Alternatively, a controller for constant power injection can be used.

Using (1) and the averaged injected DC losses, during the heating phase, an initial estimation of $C_{\text{th,core}}$ is acquired. Replacement of this value in (5) allows for calculation of $R_{\text{th,leak}}$ during the cooling phase. Finally, the corrected value of $C_{\text{th,core}}$ is calculated using (6) and division with the mass of the employed block leads to the calculation of the specific heat capacity. The maximum deviation of the specific heat capacity of MnZn N49 measured with the two proposed methods for the three values of T_{amb}, i.e., 30 °C, 55 °C, 80 °C, is 1.93 %, 0.93 %, and 0.56 %, respectively.

The expression for $\partial P_{\text{core,est}}/\partial\delta_{C_{\text{th,core}}}$, i.e., the linear sensitivity of the estimated core losses on $\delta_{C_{\text{th,core}}}$, can be derived based on the network depicted in Fig. 2(b). For this purpose, $C_{\text{th,core}}$ is replaced by $C_{\text{th,core}}(1+\delta_{C_{\text{th,core}}})$ and

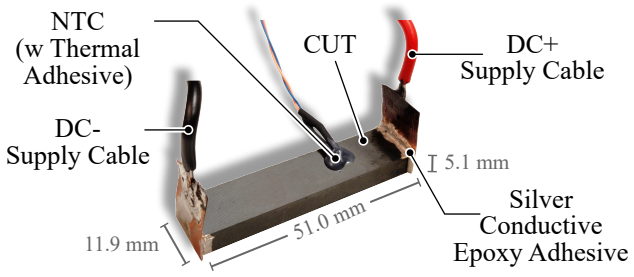

Fig. 5. N49 MnZn ferrite sample used as a DC electric conductor, for the estimation of $C_{\mathrm{th,core}}$ by means of Joule heating. The rectangular block's volume is $51.0\times11.9\times5.1\,\mathrm{mm}^3$ and its mass is 14.806 gr. The applied voltage, for all three ambient temperatures (30 °C, 55 °C, 80 °C), is fixed at 58.74 V and the injected average power is equal to 0.355 W, 0.635 W, and 1.124 W, respectively, due to the temperature dependency of ρ_{MnZn}.

$$\Delta T_{\mathrm{core}}(s) = \frac{\frac{P_{\mathrm{core}}}{s} - \frac{\Delta T_{\mathrm{core}}(s)}{R_{\mathrm{th,leak}}}}{sC_{\mathrm{th,core}}(1+\delta_{C_{\mathrm{th,core}}})}$$

$$\rightarrow \quad \Delta T_{\mathrm{core}}(t) = \mathscr{L}^{-1}\left\{\frac{P_{\mathrm{core}}}{s}\,\frac{R_{\mathrm{th,leak}}}{1+s\tau_{\mathrm{leak}}(1+\delta_{C_{\mathrm{th,core}}})}\right\}, \qquad (8)$$

results for the increase of the temperature across $C_{\mathrm{th,core}}$. Furthermore, the impact of the NTC temperature sensor on the measurement result, modeled with τ_{NTC}, is neglected, since the corresponding low-pass filter leads to a deviation between the actual and the measured temperature, which can be considered separately, cf. (13) in Section III-C. With this, $\Delta T_{\mathrm{core}}(t_1+\Delta t_1) - \Delta T_{\mathrm{core}}(t_1) = T_{\mathrm{meas}}(t_1+\Delta t_1) - T_{\mathrm{meas}}(t_1)$ applies and the time-domain function, $\Delta T_{\mathrm{core}}(t)$, can be used to evaluate (6). The result is linearized around $\delta_{C_{\mathrm{th,core}}} = 0$,

$$\left.\frac{\partial P_{\mathrm{core,est}}}{\partial \delta_{C_{\mathrm{th,core}}}}\right|_{\delta_{C_{\mathrm{th,core}}}\to 0} = \frac{P_{\mathrm{core}}}{\tau_{\mathrm{leak}}}\left(t_1 - t_{\mathrm{on}} - \frac{\Delta t_1}{-1+\mathrm{e}^{\frac{\Delta t_1}{\tau_{\mathrm{leak}}}}}\right). \qquad (9)$$

Due to $\Delta t_1 \ll \tau_{\mathrm{leak}}$, $\mathrm{e}^{\Delta t_1/\tau_{\mathrm{leak}}}$ can be approximated by $1+\Delta t_1/\tau_{\mathrm{leak}}$, and further consideration of $t_1 - t_{\mathrm{on}} \ll \tau_{\mathrm{leak}}$ leads to the expression listed in Tab. II. The other sensitivities are derived in a similar way.

B. Accuracy of the modeled leakage flux, $\delta_{R_{\mathrm{th,leak}}}$

The calculation of the worst-case uncertainty of $R_{\mathrm{th,leak}}$ is based on (5), e.g., in case of the reference experiment,

$$\begin{aligned} C_{\mathrm{th,core}}(25\,^\circ\mathrm{C}) &= 7.3\,\mathrm{J/K}, & \Delta t_2 &= 115\,\mathrm{s}, \\ T_{\mathrm{meas}}(t_2) &= 34.6\,^\circ\mathrm{C}, & T_{\mathrm{meas}}(t_2+\Delta t_2) &= 32.2\,^\circ\mathrm{C}, \end{aligned} \qquad (10)$$

apply, cf. Fig. 3. With $\delta_{C_{\mathrm{th,core}}} = \pm 3\,\%$ and $\eta_{C_{\mathrm{th,core}}} = 0.1\,\%/^\circ\mathrm{C}$, i.e., the given measurement uncertainty and the temperature dependency of $C_{\mathrm{th,core}}$, cf. Tab. II, and for a core temperature between $T_{\mathrm{amb}}+6.0\,^\circ\mathrm{C}$ and $T_{\mathrm{amb}}+8.4\,^\circ\mathrm{C}$ during $t\in[t_2, t_2+\Delta t_2]$, a worst-case range of

$$[97\,\% + 0.1\,\%/^\circ\mathrm{C}\times 6.0\,^\circ\mathrm{C},\; 103\,\% + 0.1\,\%/^\circ\mathrm{C}\times 8.4\,^\circ\mathrm{C}]\,C_{\mathrm{th,core}}, \qquad (11)$$

applies for the thermal capacitance. In addition, the measurement of the temperature difference is subject to an absolute uncertainty of $\epsilon_{T_{\mathrm{meas}}} = \pm 0.1\,^\circ\mathrm{C}$ and the uncertainty due to clock accuracy can be neglected, which leads to a minimum value of 38.7 K/W (−14 % compared to the nominal value of 45 K/W). On this basis, a conservative uncertainty of ±20 % has been considered for $\delta_{R_{\mathrm{th,leak}}}$, cf. Tab. II.

Even though, $R_{\mathrm{th,leak}}$ is subject to a comparably high uncertainty, the impact on the estimated core losses remains low, since the maximum duration of the core loss measurement, $t_{\mathrm{off}} - t_{\mathrm{on}}$ is typically in the range of 15 s to 30 s, which is much less than the time constant arising from the leakage flux, $\tau_{\mathrm{leak}} \approx 330\,\mathrm{s}$. Accordingly, the corresponding sensitivity, $\partial P_{\mathrm{core,est}}/\partial\delta_{R_{\mathrm{th,leak}}}$, is small (cf. Tab. III).

C. Impact of NTC time constant, τ_{NTC}

For the temperature measurement, the PS104J2 NTC thermistor of Littelfuse [20] is used. In order to achieve a fast response of the NTC and at the same time mechanical robustness, the temperature sensor is glued to the core using a thermally conductive adhesive (8329TFM-25ML of MG Chemicals). The CUT must be much larger in size than the temperature sensor in order to fulfill $C_{\mathrm{th,NTC}} \ll C_{\mathrm{th,core}}$ (for the case of very small cores, thermal imaging is a valid solution). An uncoated core is preferred, and in case of coating, the coating is carefully locally removed, even though it is found to have a minor impact on the measured response.

The NTC sensor features a dynamic response similar to a first-order low pass filter, cf. Fig. 3, with time constants between 3 s and 5.5 s, depending on the investigated CUT. The impact of this transfer function on the measurement result could be compensated by initial identification of the NTC time constant and application of the reciprocal of the sensor's transfer function to the measured temperature waveform. However, the additional effort that arises from the implementation of such a compensation procedure can be avoided by inserting minimum waiting times of at least $2\tau_{\mathrm{NTC}}$ between the beginning of each measurement phase and the actual measurement,

$$t_1 - t_{\mathrm{on}} > 2\tau_{\mathrm{NTC}} \quad \text{and} \quad t_2 - t_{T_{\mathrm{max}}} > 2\tau_{\mathrm{NTC}}, \qquad (12)$$

which enables small deviations between the actual core losses and the estimated core losses, $\Delta P_{\mathrm{core,NTC}}$.

A detailed inspection of $\Delta P_{\mathrm{core,NTC}}$ reveals a strong nonlinear dependency on τ_{NTC}, which renders the use of a linearized sensitivity unsuitable. Instead, $\Delta P_{\mathrm{core,NTC}}$ is directly derived based on the system's differential equation and the resulting expression for the estimated core losses (18), cf. Sec. III-I,

$$\Delta P_{\mathrm{core,NTC}} = P_{\mathrm{core}} - P_{\mathrm{core,unc}}(t_1, \Delta t_1) \approx P_{\mathrm{core}}\,\frac{\tau_{\mathrm{leak}} - t_1 - \frac{\Delta t}{2} - \frac{\tau_{\mathrm{leak}}^2}{\Delta t}\,\mathrm{e}^{-\frac{t_1}{\tau_{\mathrm{NTC}}}}}{\tau_{\mathrm{leak}} - t_1 - \frac{\Delta t}{2}}\,\frac{\tau_{\mathrm{NTC}}}{\tau_{\mathrm{leak}} - \tau_{\mathrm{NTC}}}, \qquad (13)$$

using $\epsilon_{T_{\mathrm{meas}}} = \delta_{C_{\mathrm{th,core}}} = \delta_{R_{\mathrm{th,leak}}} = 0$ and a second-order Taylor approximation for $\mathrm{e}^{-t/\tau_{\mathrm{leak}}}$. For the reference measurement and $\tau_{\mathrm{NTC}} \in [3\,\mathrm{s}, 5.5\,\mathrm{s}]$, $\Delta P_{\mathrm{core,NTC}} \in [-1.8\,\mathrm{mW}, 12.4\,\mathrm{mW}]$ results with (13), which corresponds to relatively small deviations between −0.12 % and 0.81 %. It should be pointed out

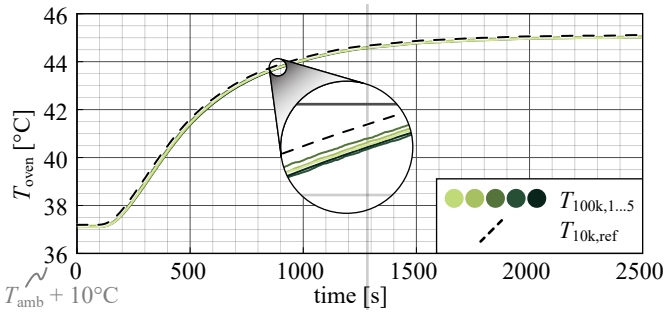

Fig. 6. Temperatures of five PS104J2 NTC thermistors from Littelfuse [20], $T_{100k,1...5}$, measured using a custom analog/digital interface circuit and a reference measurement with an MC65F103AN NTC thermistor from Amphenol Advanced Sensors [29], $T_{10k,ref}$, using a 34410A digital multimeter from Keysight Technologies [30]. All sensors are thermally coupled and covered inside an enclosure in order to limit convection; the complete setup is located inside a laboratory oven and during the experiment the reference temperature changes from 37 °C to 45 °C. Due to the overlap of the temperatures of the five PS104J2 NTC thermistors, a magnified (×7.5) view is added.

that (13) remains approximately valid also in presence of further sources of uncertainties, since all other sources mainly have an impact on the slope of the time-domain characteristic of the core temperature, $T_{core}(t)$.

D. Temperature measurement accuracy, $\epsilon_{T_{meas}}$

A custom analog/digital 14-channel interface circuit is employed to process the resistance change of the NTC thermistor. Furthermore, the considered Savitzky-Golay filter reduces eventually present measurement noise. In order to assess the accuracy of this temperature measurement setup, an initial verification has been conducted with a reference temperature measurement. This is composed of a high-accuracy NTC thermistor, MC65F103AN from Amphenol Advanced Sensors [29], which provides an absolute accuracy of ±0.05 °C at 35 °C < T < 39 °C and ±0.075 °C at 39 °C < T < 42 °C, and the 34410A digital multimeter from Keysight Technologies [30], that provides a resistance reading accuracy, corresponding to an error of 1.1 mK. The result of this reference temperature measurement, $T_{10k,ref}$ (cf. **Fig. 6**), is compared simultaneously to the measurements obtained from five PS104J2 NTC thermistors that are connected to five channels of the interface circuit, $T_{100k,1..5}$ in Fig. 6. All six sensors are closely mounted together, inside an enclosure, and using thermally conductive paste, to achieve high thermal coupling and to limit convection. For the experiment a slow, controlled temperature step from 37 °C to 45 °C is conducted inside a laboratory oven (the oven requires a minimum temperature of T_{amb} + 10 °C, in order to properly stabilize the temperature).

The measurement results reveal different deviations for absolute temperature values and temperature differences. With regard to the absolute temperature, a maximum deviation of 0.22 °C is found between $T_{10k,ref}$ and $T_{100k,4}$, which could be further improved by additional calibration of the interface circuit. However, the absolute temperature is only needed to determine the values of the temperature-dependent variables P_{core}, $C_{th,core}$, and $R_{th,leak}$; for an uncertainty of less than 0.5 °C, its impact on the resulting total uncertainty is negligible (cf. $\eta_{P_{core}}$, $\eta_{C_{th,core}}$, and $\eta_{R_{th,leak}}$ listed in Tab. II). The investigated measurement method rather requires a high accuracy of the measured temperature difference, which, for $t_1 = 0$ and a duration of $\Delta t_1 = 2500$ s, in Fig. 6, gives a maximum deviation of 8 mK for the six temperature difference measurements, $T_{meas}(t_1 + \Delta t_1) - T_{meas}(t_1)$, i.e., the uncertainties arising from linearity errors of temperature measurement sensors and interface circuitry is very small. However, due to missing specifications with regard to temperature difference measurements, the authors decided to assign the specified accuracy of the PS104J2 NTC thermistor of ±0.1 °C to the measured temperature difference,

$$\Delta T_{meas,unc} = T_{meas}(t_1 + \Delta t_1) - T_{meas}(t_1) + \epsilon_{T_{meas}},$$
$$\epsilon_{T_{meas}} = \pm 0.1\,°C, \quad (14)$$

which allows for a conservative consideration of the corresponding uncertainty.

Accordingly, and with respect to (6), the relative uncertainty of the measured core losses decreases for increasing temperature differences and reaches values of less than 2 % for temperatures differences greater than 5 °C.

E. Clock accuracy, $\epsilon_{t_{meas}}$

The considered measurement setup employs a microcontroller that is operated with an oscillator, which features a frequency stability of ±100 ppm. Accordingly, and with respect to the values given in Tab. II, the uncertainty due to a time measurement error is of low value and low sensitivity and is neglected due to this reason.

F. Temperature dependencies ($\eta_{P_{core}}$, $\eta_{C_{th,core}}$, $\eta_{R_{th,leak}}$)

All three fundamental elements of the equivalent circuit in Fig. 2 (i.e., P_{core}, $C_{th,core}$, $R_{th,leak}$) are temperature and, hence, in the considered case time dependent. The temperature dependencies of P_{core} and $C_{th,core}$ are properties of the core material, which are especially pronounced for ferrites, and the temperature dependency of $R_{th,leak}$ is due to the heat transfer mechanisms of convection and radiation. The value of $\eta_{P_{core}}$ displayed in Tab. II is determined based on the *Relative core losses versus temperature* plot of the material's datasheet [31] at $f = 500$ kHz, $B_{pk} = 100$ mT, and for $T \in [25\,°C, 40\,°C]$. The value of $\eta_{C_{th,core}}$ is determined from the measured specific heat capacity of N49 depicted in Fig. 4 and the value of $\eta_{R_{th,leak}}$ is determined based on an evaluation of the temperature dependencies of the thermal leakage flux components due to convection and radiation, considering a horizontally mounted core and using the simplified expressions given in [32].

According to Tab. II, the expressions for computing the linear sensitivities of the measured core losses with respect to $\eta_{P_{core}}$, $\eta_{C_{th,core}}$, and $\eta_{R_{th,leak}}$ are inversely proportional to $C_{th,core}$, which further confirms that an accurate knowledge of $C_{th,core}$ is indispensable to achieve an accurate measurement result.

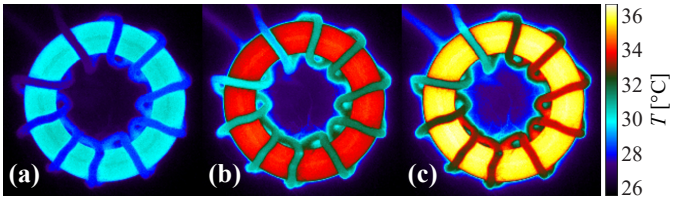

Fig. 7. Temperature monitoring of a toroidal ferrite core (R 22.1/13.7/7.9, N49) that is subject to a sinusoidal flux density of 500 kHz and 100 mT, using the FLIR A655sc IR camera. At an ambient temperature of 26.2 °C, the three depicted frames correspond to the temperatures (a) 30 °C, (b) 34 °C, (c) 36 °C. For all temperatures the maximum deviation between the points of lowest and highest temperatures in radial direction of the core is below 0.3 °C (camera resolution: 640 × 480 - pixel dimensions: $0.136 \times 0.136\,\mathrm{mm}^2$). The complete video is included in the publication as additional multimedia.

The sensitivity $\partial P_{\mathrm{core,est}}/\partial \eta_{R_{\mathrm{th,leak}}}$ is comparably small, since the leakage flux is relatively low during the short measurement time. Accordingly, $\eta_{R_{\mathrm{th,leak}}}$ has a minor contribution to the uncertainty of P_{core} and is omitted. Furthermore, also $\eta_{C_{\mathrm{th,core}}}$ can be neglected, since $|\eta_{P_{\mathrm{core}}}| \gg |\eta_{C_{\mathrm{th,core}}}|$ and same absolute values of the sensitivities, $|\partial P_{\mathrm{core,est}}/\partial \eta_{P_{\mathrm{core}}}| = |\partial P_{\mathrm{core,est}}/\partial \eta_{C_{\mathrm{th,core}}}|$, apply. Accordingly, only $\eta_{P_{\mathrm{core}}}$ is considered in the circuit's differential equation that is examined in Section III-I, which enables a compact and yet accurate solution.

G. Inhomogeneous flux density and temperature distribution

The distribution of the flux density across the core cross section has a general impact on the determined core losses. Conversion of the induced flux into flux density is conventionally done by division of the flux by the cross section of the employed core. However, cores (toroids) typically employed for the measurement of core losses cause flux density deviations between the inner and outer radius of 60 % to 70 %. This is attributed primarily to the varying magnetic lengths between the two radius and the current carrying conductors, according to the Biot-Savart law and/or the Ampere's law, and secondarily to the impact of the flux density on the relative permeability of ferrite materials. This deviation, raised to a typical power of $\beta \approx 2.5$, results in a ratio of the maximum and the minimum losses in radial core direction of more than 3. Therefore, it is advised to consider cores with slim profiles, in order to limit differences in flux density and corresponding loss densities.

Despite the inhomogeneous loss distribution in the CUT, thermal imaging reveals that the temperature gradient inside the core is negligible, cf. **Fig. 7**, due to the relatively high thermal conductivity of ferrite [$\lambda \geq 3.5\,\mathrm{W/(mK)}$]. As a result, and similar to the electric measurement of the core losses, the investigated procedure does not measure the local loss density but rather the total core losses. Furthermore, $R_{\mathrm{th,core}}$ in Fig. 2(a) can be omitted.

H. Impact of copper losses

Copper losses in the coil cause additional heating of the core and need to be limited, e.g., to a maximum of one tenth of the core losses, which is found to be easily achieved with proper choice of the CUT design parameters (e.g., core geometry, number of turns, type of conductor). In order to further minimize this effect, a thermally isolating interface tape ($\approx 0.3\,\mathrm{mm}$) can be placed between the coil and the core. The impact of the distance between coil and core on the flux distribution inside the core is negligible for core materials with high relative permeabilities, e.g., MnZn ferrite materials with $\mu_{\mathrm{r}} > 1000$. It may become more critical for high frequency NiZn ferrite materials, whose relative permeabilities can be as low as 40. FEM simulations of the high-frequency inductors that are experimentally evaluated in Section V-C and which employ the NiZn ferrite material 67 of Fair-Rite, however, confirm that the effect of the winding current on the distribution of the flux density remains negligible.

I. Total uncertainty

The total uncertainty of the measured core losses is determined based on the differential equation of the circuit depicted in Fig. 2(b),

$$C_{\mathrm{unc}} \frac{\mathrm{d}T_{\mathrm{core}}}{\mathrm{d}t} = P_{\mathrm{core}}\left[1 + \eta_{P_{\mathrm{core}}}\left(T_{\mathrm{core}} - T_{\mathrm{amb}}\right)\right] - \frac{T_{\mathrm{core}} - T_{\mathrm{amb}}}{R_{\mathrm{unc}}}, \quad (15)$$

$$C_{\mathrm{unc}} = C_{\mathrm{th,core}}\left(1 + \delta_{C_{\mathrm{th,core}}}\right), \; R_{\mathrm{unc}} = R_{\mathrm{th,leak}}\left(1 + \delta_{R_{\mathrm{th,leak}}}\right), \quad (16)$$

which, in accordance to Sections III-A, III-B, and III-F, takes the uncertainties $\delta_{C_{\mathrm{th,core}}}$, $\delta_{R_{\mathrm{th,leak}}}$, and $\eta_{P_{\mathrm{core}}}$ into consideration. Furthermore, the measured temperature is subject to the transient response of the NTC sensor, i.e., for the assumption of $C_{\mathrm{th,NTC}} \ll C_{\mathrm{th,core}}$,

$$T_{\mathrm{meas}} = T_{\mathrm{core}} - \frac{\mathrm{d}T_{\mathrm{meas}}}{\mathrm{d}t}\tau_{\mathrm{NTC}} \quad (17)$$

applies [with (22) and (23), Appendix A. gives the corresponding solutions for $T_{\mathrm{core}}(t)$ and $T_{\mathrm{meas}}(t)$, respectively].

Finally, for the estimation of the core losses according to (6), also the temperature measurement uncertainty needs to be considered,

$$P_{\mathrm{core,unc}}(t_1, \Delta t_1) = \frac{T_{\mathrm{meas}}(t_1 + \Delta t_1) - T_{\mathrm{meas}}(t_1) \pm \epsilon_{T_{\mathrm{meas}}}}{\left(\mathrm{e}^{-\frac{t_1 - t_{\mathrm{on}}}{\tau_{\mathrm{leak}}}} - \mathrm{e}^{-\frac{t_1 + \Delta t_1 - t_{\mathrm{on}}}{\tau_{\mathrm{leak}}}}\right) R_{\mathrm{th,leak}}}, \quad (18)$$

leading to a relative total uncertainty of

$$unc_{\mathrm{meas,\%}}(t_1, \Delta t_1) = 100\,\% \times \left| \frac{P_{\mathrm{core,unc}}(t_1, \Delta t_1) - P_{\mathrm{core}}}{P_{\mathrm{core}}} \right|. \quad (19)$$

Fig. 8 presents a contour plot of the worst-case values of the total uncertainty, $unc_{\mathrm{meas,\%}}$, obtained for the reference experiment defined in Tab. I, as a function of t_1 and Δt_1 ($t_{\mathrm{on}} = 0\,\mathrm{s}$ is considered). The presented plot is computed with (19) and takes the ranges of $\delta_{R_{\mathrm{th,leak}}}$, $\eta_{P_{\mathrm{core}}}$, τ_{NTC}, and

$\epsilon_{T_{\mathrm{meas}}}$, listed in Tab. II, into account.[3] For an optimal selection of t_1 and Δt_1, the total uncertainty of the measurement method is below 12 %. In addition, the region around the optimal point is substantially flat and is found to occur approximately at

$$t_{1,\mathrm{opt}} \approx 2\tau_{\mathrm{NTC}}, \quad \Delta t_{1,\mathrm{opt}} \approx \min\left(\frac{C_{\mathrm{th,core}}}{P_{\mathrm{core}}}\sqrt{\left|\frac{2\epsilon_{T_{\mathrm{meas}}}}{\eta_{P_{\mathrm{core}}}}\right|}, \Delta t_{1,\mathrm{max}}\right), \tag{20}$$

which is detailed in Appendix B. and applies if $\epsilon_{T_{\mathrm{meas}}}$ and $\eta_{P_{\mathrm{core}}}$ are dominating sources of uncertainties (the value of $\Delta t_{1,\mathrm{opt}}$ is limited to $\Delta t_{1,\mathrm{max}} = 250\,\mathrm{s}$ in order to prevent unreasonably long measurement times in case of low losses).

Due to the many uncertainty variables that have an influence on $unc_{\mathrm{meas},\%}$, it is unlikely for the worst case to happen. In a more realistic approach, a Gaussian distribution of each uncertainty is considered such that 95 % of the samples lie within the uncertainty values of Tab. II. Based on a Monte Carlo simulation approach according to [33], featuring 5000 individual simulations, the probability density function of the total uncertainty presented in **Fig. 9** is obtained for the settings of the reference experiment and optimal timing values of t_1 and Δt_1, derived similar to Fig. 8. It is found that an approximately Gaussian distribution results for $unc_{\mathrm{meas},\%}$, which is due to the fact that the total uncertainty is approximately proportional to the values of the individual uncertainty variables (except for τ_{NTC} and $\delta_{R_{\mathrm{th,leak}}}$). The negative mean value of $\mu = -4.3\,\%$ results mainly due to the negative temperature coefficient of the core losses [μ of approximately zero would result if the measured core losses were referred to a core temperature of $T_{\mathrm{meas}}(t_1 + \Delta t_1/2)$]; for a confidence interval of 95 %, $\mu \pm 2\sigma$, the total uncertainty is between $-7.4\,\%$ and $-1.1\,\%$.

The CUT defined in Tab. I has been examined with regard to different levels of core losses, ranging from 20 mW to 20 W, in order to determine the range of core losses that lead to a worst-case value of $unc_{\mathrm{meas},\%} < 20\,\%$ (cf. **Fig. 10**). Core-loss dependent optimal timing parameters, $t_{1,\mathrm{opt}}(P_{\mathrm{core}})$ and $\Delta t_{1,\mathrm{opt}}(P_{\mathrm{core}})$, have been used in this plot to enable a meaningful assessment of the achievable total uncertainty. According to the results, the method is valid from 40 mW up to 8 W, which corresponds to a value of 200 for the ratio of maximum to minimum core losses.

In case of low losses, the core temperature increases slowly and, due to the limitation of $\Delta t_{1,\mathrm{opt}}$ to $\Delta t_{1,\mathrm{max}}$, according to (20), a reduced temperature difference is measured. As a consequence, the corresponding increase of the uncertainty is mainly related to the temperature measurement error, $\epsilon_{T_{\mathrm{meas}}}$. In addition, with $\Delta t_{1,\mathrm{opt}}$ approaching τ_{leak}, also the impact of $\delta_{R_{\mathrm{th,leak}}}$, i.e., the uncertainty of $R_{\mathrm{th,leak}}$, on the total uncertainty becomes more relevant.

In case of high losses, the core temperature increases quickly. Accordingly, the increase of the total uncertainty is mainly due to the increased uncertainties arising from the temperature dependency of the core losses, $\eta_{P_{\mathrm{core}}}$, and the time constant of the NTC temperature sensor, τ_{NTC}. The two uncertainties are contradictory to each other, since the first one requires small values of t_1 and Δt_1, in order to limit the temperature increase, and the second one needs $t_1 > 2\tau_{\mathrm{NTC}}$ in order to overcome the delay error introduced by the transfer function of the NTC.

The extreme cases of core losses close to 40 mW or 8 W correspond to operating points of limited interest, i.e., insignificant introduced heat in case of low losses, which is not of practical relevance, and potential thermal runaway in case of high losses. Nevertheless, these values confine the absolute measurement limits of the specific core. Measurements of higher or lower absolute core losses are feasible for larger or smaller cores, due to the increased or decreased values of the thermal capacitance, $C_{\mathrm{th,core}}$.

IV. FEM Simulation

Section II-B details an equivalent circuit that correctly reproduces the measurement results. However, the physical validity of the circuit has not been investigated, e.g., other circuits could give similar waveforms, too. In addition, certain parameters, e.g., $R_{\mathrm{th,core}}$, depend on 3D phenomena related to the field pattern. For both these reasons, a 3D FEM simulation (COMSOL Multiphysics software [34]) of the core losses and the temperature distribution of the experimental setup is realized and the results are presented in this Section.

The model is solved in a two-step process, starting from a frequency domain Magnetic Field (MF) problem, followed by a Heat Transfer (HT) problem in the time-domain. Critical dependencies, i.e., core-loss density with respect to magnetic flux and temperature, specific heat capacity with respect to temperature, and the dependencies of different cooling mechanisms (convection and radiation) on temperature are taken into consideration. On the contrary, dependencies of less impact, e.g., temperature dependency of the core permeability and hence of the magnetic field pattern, are excluded (cf. **Fig. 11**). Solving both, MF and HT, problems in the time domain would lead to unrealistic computation times, due to the substantially different time constants of the two problems, i.e., microseconds for the MF problem and seconds for the HT problem. The implemented model corresponds to the experiment specified in Tab. I and considers the waveforms of Fig. 3, i.e., it features a toroidal core (R 22.1/13.7/7.9) made of N49 MnZn ferrite material with 10 turns of high-frequency litz wire ($180 \times 71\,\mu\mathrm{m}$) that is subject to a sinusoidal flux with a frequency of 500 kHz and an average flux density of 100 mT. The loss data for the simulations are taken from the *Magnetic Design Tool* of EPCOS-TDK [35] and for the convection mechanism, natural convection is considered. The specific heat capacity data is taken from the DSC measurement of Fig. 4.

[3] The implemented computation takes $2^5 = 32$ combinations of uncertainty values into account. Each of these values is selected such that, in case of a standalone consideration, minimum (most negative) or maximum (most positive) contribution to the total uncertainty results. With regard to $\delta_{C_{\mathrm{th,core}}}$, $\delta_{R_{\mathrm{th,leak}}}$, $\eta_{P_{\mathrm{core}}}$, and $\epsilon_{T_{\mathrm{meas}}}$, this is achieved by using the minimum and maximum boundary values of these four uncertainties. In case of τ_{NTC}, the minimum and maximum uncertainties need to be obtained numerically from (13) for each combination of t_1 and Δt_1, due to the nonlinear characteristic of (13).

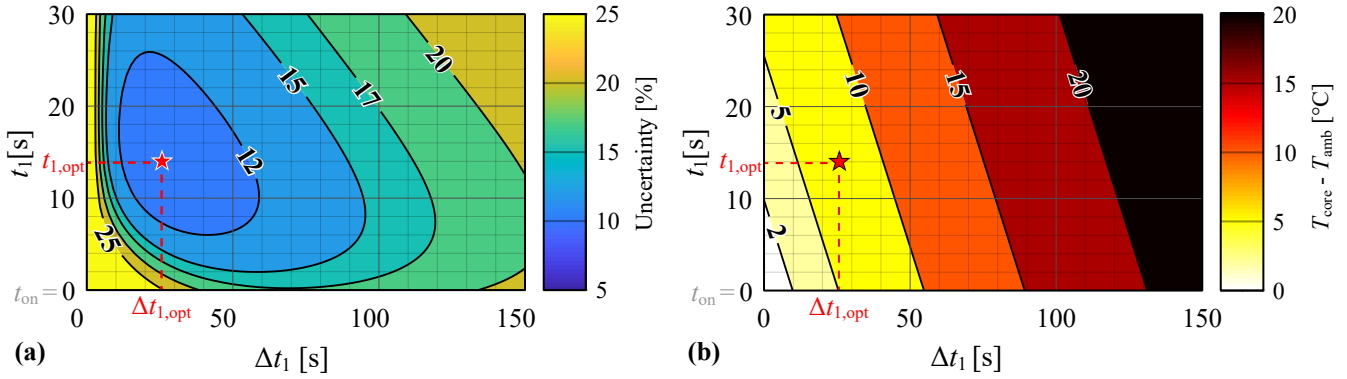

Fig. 8. (a) Worst-case total error and (b) increase of the core's temperature with respect to t_1 and Δt_1 (cf. Fig. 3) , for the specifications of Tab. I, the uncertainties of Tab. II, and the equivalent circuit of Fig. 2.

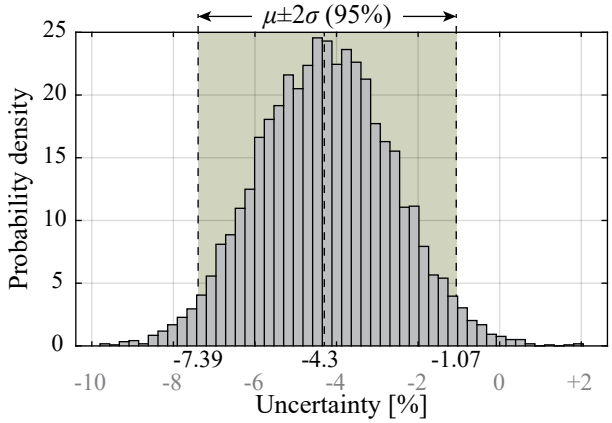

Fig. 9. Distribution of the total uncertainty resulting from a Monte Carlo simulation of the uncertainties of Tab. II and for the specifications presented in Tab. I. The uncertainties are assumed to follow a Gaussian distribution.

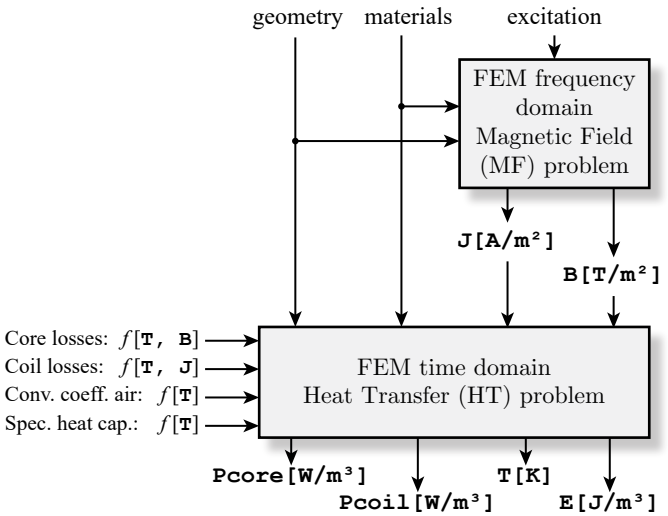

Fig. 11. Flowchart of the realized FEM model. The model is split into two subsequent problems, one in the frequency and one in the time domain. This results in a significant decrease of the computational effort, by preserving only the critical model dependencies.

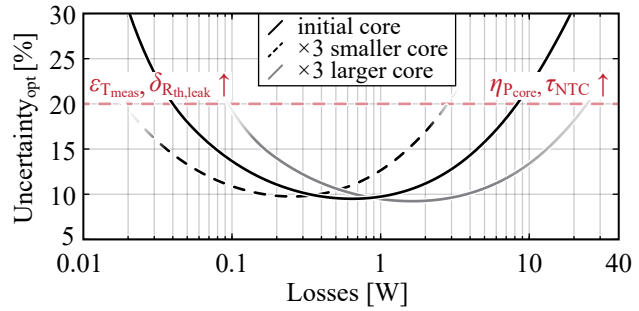

Fig. 10. Evaluation of the measurement uncertainty for a wide range of losses, i.e., between 20 mW and 20 W, for the specifications of Tab. I. For each value of P_{core} the optimal selection of t_1 and Δt_1 (cf. Fig. 3) is considered. Moreover, the same curve for a core of three times larger volume and a core of three times smaller volume is depicted.

The resulting temperature progression over time, shown in **Fig. 12(a)**, is in good agreement with the core temperature behavior of the simulated circuit, $T_{core,sim}$, of Fig. 3. **Fig. 12(b)** depicts the change of the core losses over time and reveals the high ratio of core to copper losses. Finally, **Fig. 12(c)** presents the energy distribution of the losses generated in the core and the coil, $E_{losses,core}$ and $E_{losses,coil}$, the thermal energy stored in the core, $E_{stored,core}$, and the thermal energy transferred to the ambient, $E_{stored,other}$. During the heating phase, most of the energy stays inside the core and during the cooling phase the energy is slowly passed to the ambient. However, even during the heating phase, a substantial amount of energy is leaking to the ambient, which confirms that the estimation of the core losses needs to take $R_{th,leak}$ into account.

Fig. 13 presents important values of the simulated component for the time instant of t_{off}, cf. Fig. 12. As discussed in Section III-G, Fig. 13(a) and (b) reveal a gradient of the flux density in radial direction and an even more substantial

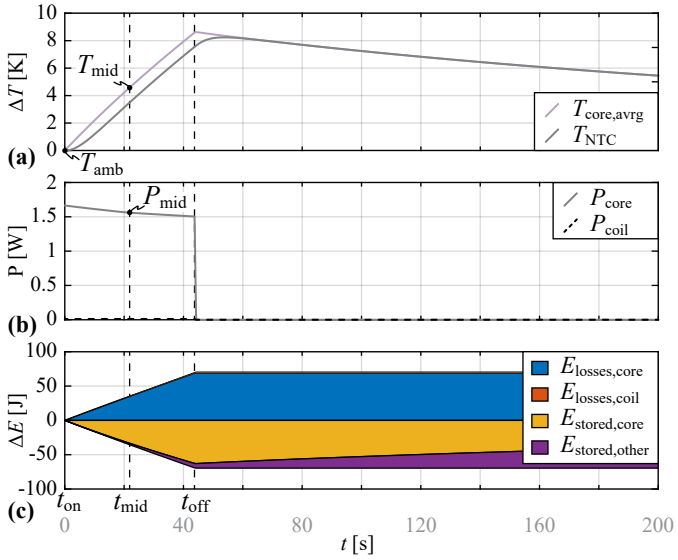

Fig. 12. Waveforms of the Heat Transfer (HT) FEM simulation in the time domain for the specifications of Tab. I. (a) Temperature change of the magnetic core and the NTC; (b) generated core and coil losses; (c) distribution of the generated losses and the stored thermal energy over time.

gradient of the core loss density, due to the raise to the power of β, with a ratio of maximum to minimum loss density of 3.8 [cf. Fig. 13(b)]. However, the impact on the core temperature gradient is negligible [$T_{\mathrm{core,max}}(t_{\mathrm{off}}) - T_{\mathrm{core,min}}(t_{\mathrm{off}}) < 0.3\,°\mathrm{C}$, cf. Fig. 13(c)], which further confirms the assumption of $R_{\mathrm{th,core}} \approx 0$. Accordingly, the stored thermal energy features a nearly homogeneous distribution, since the change in the specific heat capacity of N49 is negligible for ΔT_{core} of 0.3 °C [cf. Fig. 13(d)].

A comparison between the core losses estimated with (5), (6), and (20), using $C_{\mathrm{th,core}}$ at $T_{\mathrm{core}} = T_{\mathrm{amb}}$ and the instantaneous losses at t_{on}, results in a deviation of 9 %. Nevertheless, the comparison between the same calculation, using $C_{\mathrm{th,core}}$ at $T_{\mathrm{core}} = T_{\mathrm{mid}}$ (cf. Fig. 12) and the instantaneous losses at t_{mid}, results in a deviation of only 2 %. With this, the FEM simulation results confirm the validity of both, the equivalent circuit and the uncertainty analysis. Finally, comparison between the extraction of losses using the temperature waveform measured on the inner, middle, and outer circumference results in a maximum deviation of 0.8 %, for the simulated maximum instantaneous temperature difference of 0.3 °C, since the instantaneous deviation corresponds to a temperature offset and the temperature differences measured over time are almost identical at inner and outer circumference.

V. Experimental Verification

A. Workflow of the core loss measurements

The workflow of the complete experiment consists of three main parts, i.e., selection of the CUT, conducting the measurements, and post-processing the acquired data.

1) Selection of a suitable CUT: The selection of the CUT features two main degrees of freedom, i.e., the core volume, Vol_{core} (which translates into magnetic core length, core cross-section, average turn length, and wire diameter) and the number of turns, N. The requirement of negligible coil losses, defined with $P_{\mathrm{core}} \geq k_{\mathrm{loss}} P_{\mathrm{coil}}$, where $k_{\mathrm{loss}} \gg 1$ is the minimum acceptable ratio between P_{core} and P_{coil}, sets a lower boundary for Vol_{core}. At the other end of the scale, the maximum allowed voltage in the setup, e.g., due to insulation and safety reasons and/or equipment limitations, defines an upper boundary for the the product of $Vol_{\mathrm{core}} N$ (assuming a core cross section that is proportional to $Vol_{\mathrm{core}}^{2/3}$). Both boundaries need to be evaluated with respect to the desired measurement ranges, e.g., minimum to maximum peak flux density and frequency.

In case of cores made of NiZn materials, which feature low relative permeability (i.e. commonly below 300), it is advised to experimentally verify whether the flux distribution is equal, by measuring the voltage induced in a single turn sensing winding when moving it along the circumference of the magnetic core. In addition, it is mentioned in literature that cores of same NiZn materials but different sizes perform differently [36], therefore, the same core should be used for all considered frequencies.

Finally, it is important to consider a core with a thin profile (i.e., the value of $d_{\mathrm{out}} - d_{\mathrm{in}}$ is relatively small), in order to mitigate the error caused by the gradient of loss density in radial direction, cf. Section III-G, and to ensure that the maximum measurement frequency is less than the self-resonance frequency of the component, which limits the maximum number of turns for a given core.

2) Conducting the experiments: The experimental setup is implemented according to Section II. In case of large cores, two NTC sensors can be used (on the inner and outer circumference of the toroid) in order to monitor the homogeneity of the temperature distribution. The type of excitation is independent of the core-loss measurement method, hence, any flux waveform can be applied to the CUT and also an additional winding for DC premagnetization can be employed.

After a change in the experimental setup (e.g., reference temperature update, different core size) and during the first experiment, both the heating and the cooling phase are required for the extraction of P_{core} and $R_{\mathrm{th,leak}}$ according to (6) and (5), respectively. For subsequently acquired measurement points, it is sufficient to record only the heating phase, since $R_{\mathrm{th,leak}}$ remains constant.

3) Post-processing: In a first step, a Savitzky-Golay filter is applied to the measured temperature, in order to decrease the measurement noise without distorting the required information, as shown in **Fig. 14(a)**. The extraction of P_{loss} is based on (6) and employs the timing parameters defined with (20). Under the valid assumption of $\tau_{\mathrm{NTC}} \ll \tau_{\mathrm{leak}}$, the increase of the temperature difference $T_{\mathrm{meas}}(t) - T_{\mathrm{amb}}$ can be considered a low-pass filtered response of a ramp function. Hence, the intersection of the asymptote that results after convergence of $T_{\mathrm{meas}}(t) - T_{\mathrm{amb}}$ with the time axis yields an estimate for τ_{NTC} (assuming that $t_{\mathrm{on}} = 0$) as explained with Fig. 2.47(b) in [37]. The estimation of $R_{\mathrm{th,leak}}$ uses (5), $t_2 = t_{T_{\mathrm{max}}} + 2\tau_{\mathrm{NTC}}$, and a measurement duration, Δt_2, that

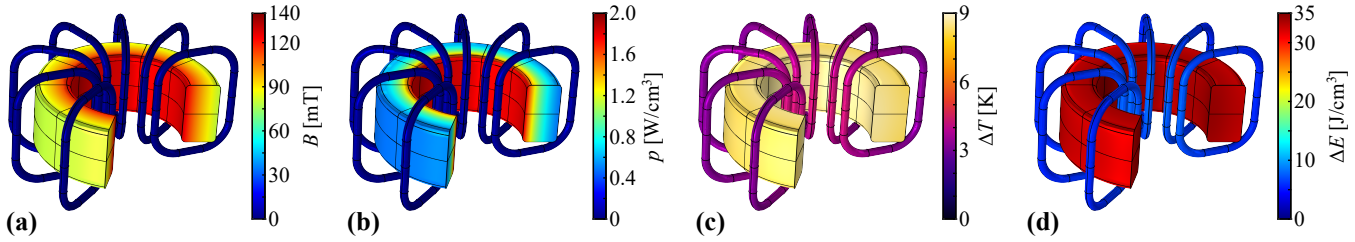

Fig. 13. FEM simulation results of a toroidal ferrite core (R 22.1/13.7/7.9, N49) with 10 turns (high frequency litz wire, 180 × 71 µm), for the specifications of the experiment of Fig. 3/Tab. I, i.e., 500 kHz/100 mT and average core losses equal to 1.54 W. The depicted result corresponds to the instant $t = t_{\text{off}}$. Distributions of: (a) flux density, (b) loss density, (c) temperature difference, (d) density of the stored thermal energy (as compared to the ambient condition).

corresponds approximately to $|\Delta T_2| \geq 30|\epsilon_{T_{\text{meas}}}| = 3\,°\text{C}$ to achieve sufficient accuracy of $\delta_{R_{\text{th,leak}}}$. Analysis similar to Fig. 8 for the extraction of $t_{2,\text{opt}}$ and $\Delta t_{2,\text{opt}}$ is possible.

B. Measurement results for MnZn ferrite cores

Fig. 14 depicts measured temperatures and core losses for ferrite N87 and N49 (EPCOS-TDK) that have been obtained with a setup according to Fig. 1. The two CUTs are R 41.8/26.2/12.5 (N87) and R 22.1/13.7/7.9 (N49) toroidal cores, having excitation coils with 15 and 10 turns, respectively, which are made of high-frequency litz wire (180 × 71 µm). Moreover, the temperature is measured according to Section III-C, by averaging of the temperatures measured by two sensors glued on the inner and outer circumference, respectively. In order to verify the accuracy of the measurement, electrical measurements are conducted as an alternative to the proposed method, employing capacitive compensation of the inductive behavior as described in [5] and shown in **Fig. 15**. For this concept, in addition to the capacitive compensation, a sense winding directly connected to a high input impedance voltage probe is used, to exclude the influence of the copper losses in R_{coil1}. Finally, a high accuracy measurement of the circuit current, i_{meas}, allows for calculation of the core losses of the CUT using

$$P_{\text{CUT}} = I_{\text{meas,rms}} V_{\text{meas,rms}}. \tag{21}$$

For each measured point an error analysis has been conducted for both methods in order to verify the accuracies of the measurements.

The average absolute deviation between the two methods for all measurements is less than 5.0 % and the maximum absolute deviation is below 13.0 %, both of which confirm the validity of the method. More interestingly, the proposed method is successfully applied to a wide range of losses between 45 mW to 4.5 W. Finally, it can be observed that with increasing frequency the uncertainty range of the electrical measurements, even for the case of capacitive compensation of the reactive power, starts exceeding the one of the proposed method, mainly due to the error introduced by the measurement equipment. This confirms the significance of the transient calorimetric method especially for measurements of NiZn in the MHz range.

C. Measurement results for NiZn ferrite cores

For the measurement of NiZn ferrite cores, the core R 21/13/6.4 with material 67 (Fair-Rite, manufacturer no: 5967000601) has been used. Due to its thin profile, a single NTC sensor glued on the middle circumference is used. The measurement circuit employed is depicted in **Fig. 16**. The input signal, which is generated with the waveStation 2052 signal generator from Teledyne LeCroy [39], is amplified with the AR 150A100D RF power amplifier [40]. A custom made impedance matching transformer, realized with a R 32/19/9.5 toroidal core with material 67 (Fair-Rite, manufacturer no: 5967001701) and a turns ratio of 12:3 is used in order to increase the load impedance on the primary side (i.e., RF amplifier side) and provide galvanic isolation between the amplifier and the core loss measurement circuit. For each considered CUT, resonance matching capacitors of type MC from Cornell Dubilier Electronics [41] with mica dielectric are used. The specific capacitors are suitable for RF applications in the MHz range. The proposed circuit is required to achieve sufficient impedance matching for the amplifier and, with this, stable operation, and is not relevant for the proposed transient calorimetric measurement method. Hence, provided that the required voltage, V_{CUT}, is applied to the CUT, operation directly at the resonant frequency is not required. Finally, a sensing winding is used to monitor the flux in the core, since the low relative permeability of the 67, $\mu_{\text{r}} \approx 40$, leads to low coupling (cf. Section V-A1).

For the acquirement of the loss-data of Fair-Rite 67 NiZn material, the same core has been used during the complete measurement procedure. However, depending on the measured frequency range, the number of turns has been adapted in order to limit the required RMS voltage to values of less than 120 V. Voltage measurement in this frequency range, i.e., 5 MHz to 50 MHz, requires a careful selection of the equipment. In case of the discussed experiments, the *PHV 1000-RO* passive probe (by PMK) has been used, since the selected probe can measure two to three times higher voltages at 50 MHz than other state-of-the-art high frequency passive probes, i.e., up to 150 V RMS. However, it has a parasitic input capacitance of 8 pF, which at this frequency range leads to non-negligible currents through the probe and also affects the resonance frequency of the circuit. Nevertheless, in case of the proposed method, this impact

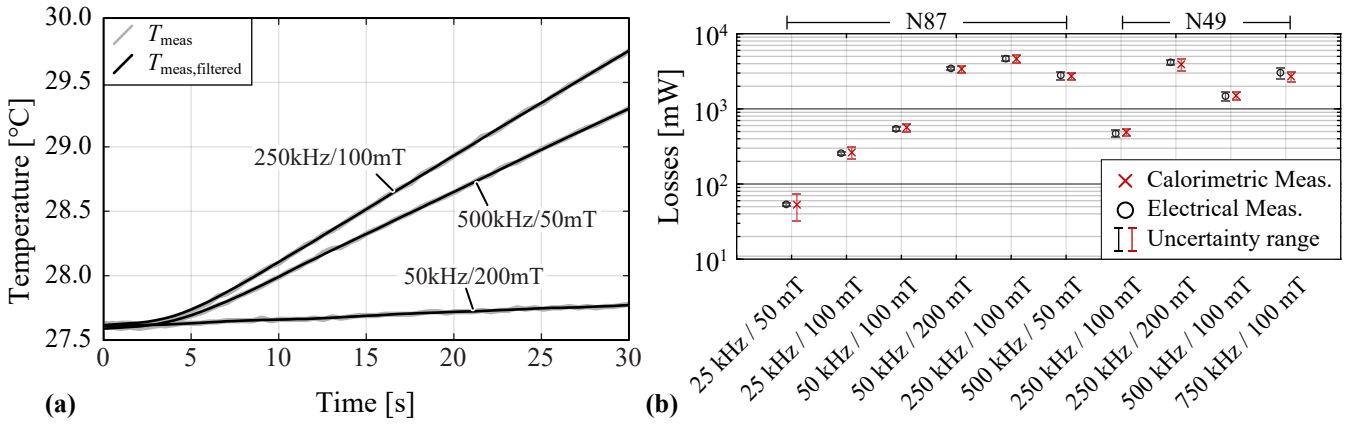

Fig. 14. (a) Comparison of waveforms of three different measurements of Ferrite N87, before and after application of the Savitzky-Golay filter; (b) comparison of the accuracies achieved with the proposed calorimetric method and the electric method described in [5] for two different DUTs, i.e., R 41.8/26.2/12.5 - N87 and R 22.1/13.7/7.9 - N49, and for ambient temperature between 26 °C and 28 °C.

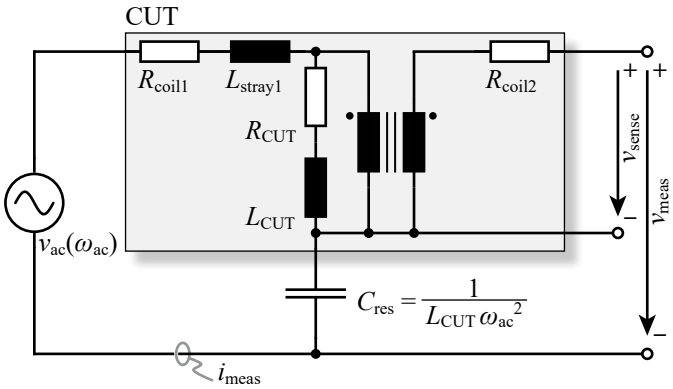

Fig. 15. Electrical circuit according to [5], used for the purpose of experimental verification, cf. Fig. 14(b). Examples of the same setup can be also found in [7], [9]. For the measurements, the following equipment from Teledyne LeCroy was used: PP018-1 passive probe (v_{meas}), ADP305 differential probe (v_{sense}), AP015 current probe (i_{meas}) and all together were connected to HDO4054A oscilloscope [38].

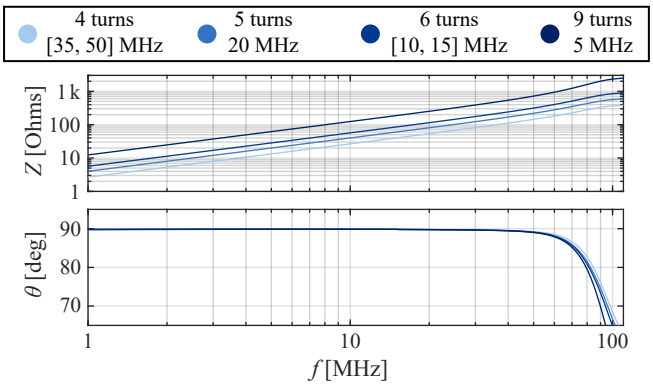

Fig. 17. Impedance measurement, using the high precision impedance analyzer 4294A from Agilent, of the R 21/13/6.4 Fair-Rite 67 NiZn core for different number of turns. For the coil a flat-wire, 3.175 mm × 0.137 mm, is used.

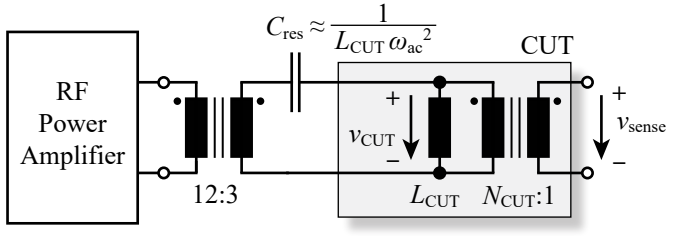

Fig. 16. Electrical circuit employed for the measurement of core losses of Fair-Rite 67 NiZn material. The setup is required only in order to achieve a better impedance matching for the 50 Ω output of the RF amplifier and not directly for the transient calorimetric measurement method.

is of minor relevance. In order to ensure flat response of the probe at the complete frequency range, compensation of the probe individually for each measured frequency is important.

In **Fig. 17** the measured impedances of the CUT for different number of turns are depicted. The abrupt change of the cores' behavior at 60 MHz is in consistence with the real and imaginary relative permeability values of the material's datasheet [36]. According to this result, core loss measurements up to 50 MHz are clearly feasible, since no resonance issues exist and at 50 MHz the phase angle is still greater than 89.3 °.

Fair-Rite 67 NiZn is a perminvar material, i.e., in case high enough magnetic field or strong enough mechanical shock is applied to the core, it will change its magnetic properties in an irreversible way [42]. Therefore, when measuring such material, it is advised to repeat the initial measurements, i.e., impedance measurement and/or first loss-measurement points, after all the points of interest have been measured, in order to confirm that the material was not over-stressed by accident and hence preserves its initial properties and the measurements are valid.

The complete measured loss-map of the material at 25 °C is shown in **Fig. 18**. According to the results, the maximum frequency for practical use is 20 MHz, since above this frequency the value of α (Steinmetz equation) increases abruptly. This is consistent with the small signal imaginary

part of the permeability shown in the material's data sheet [36]. Steinmetz parameters of $k = 1.36 \times 10^{-10}$, $\alpha = 1.4$, and $\beta = 2.4$ provide a good approximation of the measured losses in the frequency range between 5 MHz and 20 MHz, with a maximum and average error of 17 % and 4.5 %, respectively. Above 20 MHz, different Steinmetz parameters are required due to the increase of α.

Due to the nature of the proposed method, the measurement uncertainty is independent of the type of excitation, e.g., the worst-case uncertainty for the challenging measurements at 50 MHz is below 15 %. Overall, the measurements of Fig. 18 feature a maximum and an average worst-case uncertainty of 19.8 % and 13.3 %, respectively.

VI. Conclusion

This paper presents a transient calorimetric method for measuring the losses of ferrite cores independent of the type of excitation, with or without premagnetization. The method relies upon the correlation between the measured rate of rise of the core temperature over time, the core's thermal capacitance and the introduced losses. Accurately measured specific heat capacities of four commonly used ferrite core materials, using a Differential Scanning Calorimeter (DSC), are provided. The main sources of inaccuracy are analyzed and, with this, the total measurement uncertainty is evaluated. The analytical findings are supported based on a proposed thermal equivalent circuit, FEM simulations, and thermal imaging using a high resolution IR camera. In addition, a step-by-step description of the workflow for conducting the experiments is given.

The method is initially applied to commonly used N87 and N49 MnZn ferrite materials of EPCOS-TDK, and the results of thermal measurement are verified by electrical measurements. For all measurements, the deviations between the measured and the reference values are below 13 %, which is within the typical tolerance of cores produced in different batches and also within the commonly accepted accuracy for the execution of a complete component optimization. Finally, the method is applied to the 67 NiZn material of Fair-Rite for frequencies up to 50 MHz. With total measurement uncertainties of less than 20 %, the transient calorimetric method demonstrates its great strength compared to electrical methods, which would be very difficult to realize at these high frequencies. Based on the acquired loss-map, Steinmetz parameters are provided that accurately describe the material up to 20 MHz.

Acknowledgment

The authors would like to thank Dr. Kirill Feldman of the Soft Materials Laboratory of ETH Zurich, for supporting this work with providing his expertise in materials science and for conducting the specific heat capacity measurements using the Differential Scanning Calorimeter (DSC) method. Furthermore, the comprehensive support of the Fair-Rite Products Corporation (Mr. John Lynch) with samples of NiZn ferrite cores, detailed core loss data and further core material characteristics is thankfully acknowledged. Finally, the authors acknowledge the contribution of Prof. Alex J. Hanson of University of Texas at Austin, for sharing his experience on electrical measurements in the MHz range.

Appendix

In the Apendix, the resulting expressions of the derivation of the total uncertainty equation employed in Section III-I are provided.

A. Derivation of total uncertainty

The solution of the differential equation (15) is:

$$T_{\mathrm{core}}(t) = -\frac{T_{\mathrm{amb}}}{P_{\mathrm{core}}\eta_{P_{\mathrm{core}}}R_{\mathrm{unc}}-1} + \frac{P_{\mathrm{core}}R_{\mathrm{unc}}\left(\mathrm{e}^{\frac{\left(P_{\mathrm{core}}\eta_{P_{\mathrm{core}}}R_{\mathrm{unc}}-1\right)t}{R_{\mathrm{unc}}C_{\mathrm{unc}}}} + \eta_{P_{\mathrm{core}}}T_{\mathrm{amb}} - 1\right)}{P_{\mathrm{core}}\eta_{P_{\mathrm{core}}}R_{\mathrm{unc}}-1}. \quad (22)$$

Solution of the differential equation (17), taking solution (22) into account (cf. Tab. II):

$$T_{\mathrm{meas}}(t) = \frac{\mathrm{e}^{-\frac{t}{\tau_{\mathrm{NTC}}}}}{\left(P_{\mathrm{core}}\eta_{P_{\mathrm{core}}}R_{\mathrm{unc}}-1\right)} \frac{1}{\left[C_{\mathrm{unc}}R_{\mathrm{unc}} + \left(P_{\mathrm{core}}\eta_{P_{\mathrm{core}}}R_{\mathrm{unc}}-1\right)\tau_{\mathrm{NTC}}\right]} \Bigg(\left(P_{\mathrm{core}}\eta_{P_{\mathrm{core}}}R_{\mathrm{unc}}-1\right)P_{\mathrm{core}}R_{\mathrm{unc}}\tau_{\mathrm{NTC}} + \mathrm{e}^{\frac{t}{\tau_{\mathrm{NTC}}}} \Bigg\{ C_{\mathrm{unc}}P_{\mathrm{core}}R_{\mathrm{unc}}^2\mathrm{e}^{\frac{\left(P_{\mathrm{core}}\eta_{P_{\mathrm{core}}}R_{\mathrm{unc}}-1\right)t}{C_{\mathrm{unc}}R_{\mathrm{unc}}}} + + \left[C_{\mathrm{unc}}R_{\mathrm{unc}} + \left(P_{\mathrm{core}}\eta_{P_{\mathrm{core}}}R_{\mathrm{unc}}-1\right)\tau_{\mathrm{NTC}}\right] \left[\left(\eta_{P_{\mathrm{core}}}T_{\mathrm{amb}}-1\right)P_{\mathrm{core}}R_{\mathrm{unc}}\tau_{\mathrm{NTC}} - T_{\mathrm{amb}}\right] \Bigg\} \Bigg). \quad (23)$$

B. Derivation of optimal measurement times

It is found that nearly minimum total uncertainty can be achieved with

$$t_{1,\mathrm{opt}} \approx 2\tau_{\mathrm{NTC}}, \quad (24)$$

which mainly mitigates the uncertainty that arises from the time constant of the NTC. With regard to the measurement duration, Δt_1, the evaluation of all sensitivities listed in Tab. II, based on the values given in Tab. I, reveals that $\epsilon_{T_{\mathrm{meas}}}$ and $\eta_{P_{\mathrm{core}}}$ are dominating sources of time-dependent uncertainties.[4] Summation of these two uncertainties and minimization with respect to Δt_1 provides an approximation of $\Delta t_{1,\mathrm{opt}}$,

$$unc_{\Delta t_1}(\Delta t_1) \approx \left|\eta_{P_{\mathrm{core}}}\right| \frac{P_{\mathrm{core}}^2\left(\Delta t_1 + 2\left(t_1 - t_{\mathrm{on}}\right)\right)}{2\,C_{\mathrm{th,core}}} + \left|\epsilon_{T_{\mathrm{meas}}}\right| \frac{C_{\mathrm{th,core}}}{\Delta t_1}, \quad (25)$$

$$\frac{\partial unc_{\Delta t_1}(\Delta t_{1,\mathrm{opt}})}{\partial \Delta t_{1,\mathrm{opt}}} = 0 \Rightarrow \Delta t_{1,\mathrm{opt}} = \frac{C_{\mathrm{th,core}}}{P_{\mathrm{core}}}\sqrt{\left|\frac{2\epsilon_{T_{\mathrm{meas}}}}{\eta_{P_{\mathrm{core}}}}\right|}. \quad (26)$$

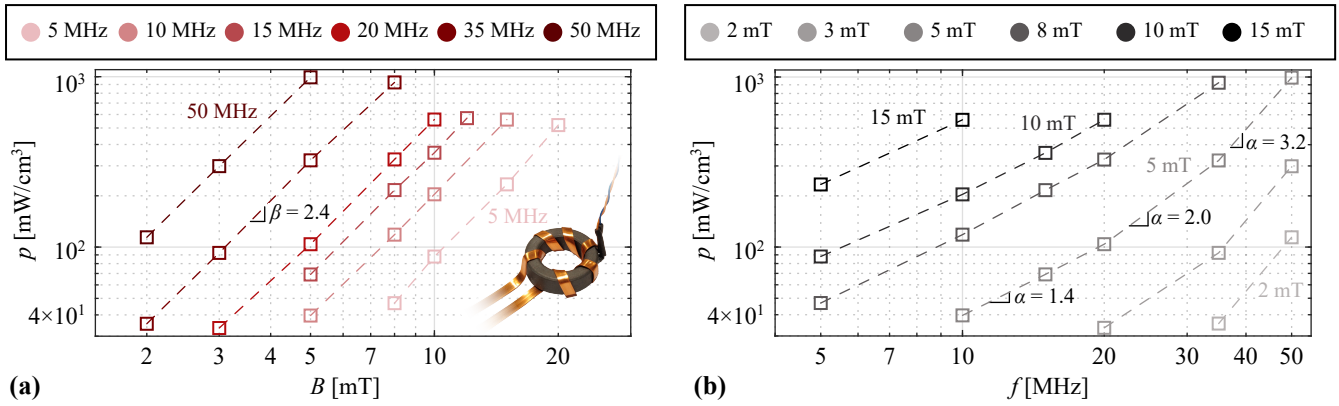

Fig. 18. Measured loss density of Fair-Rite 67 at 25 °C (a) with respect to magnetic flux and (b) with respect to frequency. The losses are measured using a R 21/13/6.4 (manufacturer no: 5967000601) magnetic core. The fitted Steinmetz parameters, $k = 1.36 \times 10^{-10}$, $\alpha = 1.4$, and $\beta = 2.4$, result in a maximum and an average error of 17 % and 4.5 %, respectively, and are valid for frequencies up to 20 MHz. Above this frequency, different Steinmetz parameters are required due to the increase in α. The measurements feature a maximum and an average worst-case measurement uncertainty of 19.8 % and 13.3 %, respectively.

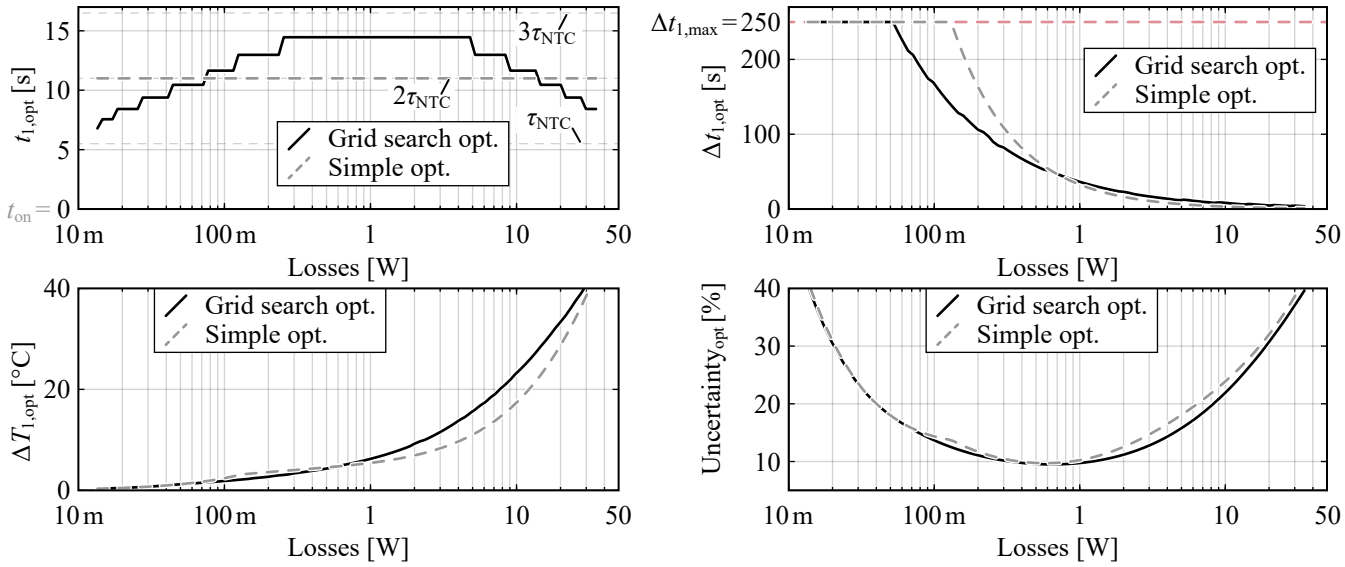

Fig. 19. Comparison of the results obtained with a numerically expensive grid-search approach and the presented simplification, for the optimal selection of t_1 (24) and Δt_1 (26) (cf. Fig. 3), which is required for the estimation of the measured core losses using (6). For the complete range of losses $t_{1,\mathrm{opt}}$ stays within τ_{NTC} and $3\tau_{\mathrm{NTC}}$, hence confirming (20). The maximum deviation of the measurement uncertainty between the two approaches is below 14 %.

Fig. 19 presents a comparison between $t_{1,\mathrm{opt}}$ and $\Delta t_{1,\mathrm{opt}}$ determined with a grid-search and the simplified expressions, for the range of losses considered in Fig. 10. The result for the achieved measurement uncertainty reveals an average deviation of less than 14 %. However, long measurement durations at low losses cause a violation of the initial assumption that $\Delta t_1 \ll \tau_{\mathrm{leak}}$ applies. Accordingly, the results for accurate and simplified values of $\Delta t_{1,\mathrm{opt}}$ differ substantially at low losses. Still, the impact on the total error is low, since the resulting uncertainty maps are highly flat at these loss-levels.

[4] If the uncertainty due to $\eta_{P_{\mathrm{core}}}$ is excessively greater than the uncertainty arising from $\epsilon_{T_{\mathrm{meas}}}$ at the tested operating point, it is found that the corresponding loss density is very high.

References

[1] B. Carsten, "Waveforms for stimulating magnetic cores," *Presentation at the PSMA Magnetics Committee / IEEE PELS High Frequency Magnetics Workshop*, March 2017.

[2] V. J. Thottuvelil, T. G. Wilson, and H. A. Owen, "High-frequency measurement techniques for magnetic cores," in *Proc. of the IEEE Power Electronics Specialists Conf. (PESC)*, June 1985, pp. 412–425.

[3] B. Carsten, "Fast, accurate measurement of core loss at high frequencies," in *Proc. of the Int. Conf. on Power Conversion and Intelligent Motion (PCIM)*, March 1986, pp. 29–33.

[4] J. Zhang, G. Skutt, and F. C. Lee, "Some practical issues related to core loss measurement using impedance analyzer approach," in *Proc. of the IEEE Applied Power Electronics Conf. and Expo. (APEC)*, vol. 2, March 1995, pp. 547–553.

[5] Z. Daming, S. Birlasekaran, S. T. Tang, and H. P. Cheng, "Ferrite core loss measurement with arbitrary wave excitation," in *Proc. of the IEEE International Conf. on Power System Technology (PowerCon)*, vol. 1, Nov. 2004, pp. 564–567.

[6] M. Mu, F. C. Lee, Q. Li, D. Gilham, and K. D. T. Ngo, "A high frequency core loss measurement method for arbitrary excitations," in *Proc. of the IEEE Applied Power Electronics Conf. and Expo. (APEC)*, March 2011, pp. 157–162.

[7] M. Mu, Q. Li, D. J. Gilham, F. C. Lee, and K. D. T. Ngo, "New core loss measurement method for high-frequency magnetic materials," *IEEE Trans. Power Electron.*, vol. 29, no. 8, pp. 4374–4381, Aug 2014.

[8] C. R. Sullivan, "Survey of core loss test methods," (accessed July 19, 2019). [Online]. Available: http://sites.dartmouth.edu/power-magnetics/files/2017/03/Survey-of-Core-Loss-Test-Methods-Sullivan.pdf

[9] A. J. Hanson, J. A. Belk, S. Lim, C. R. Sullivan, and D. J. Perreault, "Measurements and performance factor comparisons of magnetic materials at high frequency," *IEEE Trans. Power Electron.*, vol. 31, no. 11, pp. 7909–7925, Nov 2016.

[10] D. Hou, M. Mu, F. C. Lee, and Q. Li, "New high-frequency core loss measurement method with partial cancellation concept," *IEEE Trans. Power Electron.*, vol. 32, no. 4, pp. 2987–2994, April 2017.

[11] F. Zhu, Q. Li, and F. C. Lee, "Improved partial cancellation method for high frequency core loss measurement," in *Proc. of the IEEE Applied Power Electronics Conf. and Expo. (APEC)*, March 2019, pp. 1430–1435.

[12] T. Kleeb, B. Dombert, S. Araújo, and P. Zacharias, "Loss measurement of magnetic components under real application conditions," in *Proc. of the IEEE European Power Electronics and Application Conf. (EPE-ECCE Europe)*, Sep. 2013, pp. 1–10.

[13] P. Papamanolis, F. Krismer, and J. W. Kolar, "Minimum loss operation of high-frequency inductors," in *Proc. of the IEEE Applied Power Electronics Conf. and Expo. (APEC)*, March 2018, pp. 1756–1763.

[14] C. Xiao, G. Chen, and W. G. H. Odendaal, "Overview of power loss measurement techniques in power electronics systems," *IEEE Trans. Ind. Appl.*, vol. 43, no. 3, pp. 657–664, May 2007.

[15] D. Rothmund, D. Bortis, and J. W. Kolar, "Accurate transient calorimetric measurement of soft-switching losses of 10-kV SiC MOSFETs and diodes," *IEEE Trans. Power Electron.*, vol. 33, no. 6, pp. 5240–5250, 2018.

[16] J. K. Bowman, R. F. Cascio, M. P. Sayani, and T. G. Wilson, "A calorimetric method for measurement of total loss in a power transformer," in *Proc. of the IEEE Power Electronics Specialists Conf. (PESC)*, June 1991, pp. 633–640.

[17] T. Komma and H. Gueldner, "A method of determining core losses caused by a DC flux-density bias," in *Proc. of the Int. Conf. on Power Conversion and Intelligent Motion (PCIM)*, March 2002, pp. 215–220.

[18] V. Loyau, M. LoBue, and F. Mazaleyrat, "Comparison of losses measurement in a ferrite with two calorimetric methods," *IEEE Trans. Magn.*, vol. 46, no. 2, pp. 529–531, 2010.

[19] A. Savitzky and M. J. E. Golay, "Smoothing and Differentiation of Data by Simplified Least Squares Procedures," *Analytical Chemistry*, vol. 36, no. 8, p. 1627–1639, July 1964.

[20] "PS104J2 - PS Series," (accessed Nov. 19, 2019). [Online]. Available: https://www.littelfuse.com/products/temperature-sensors/leaded-thermistors/interchangeable-thermistors/standard-precision-ps/ps104j2.aspx

[21] "HIGH-RESOLUTION SCIENCE GRADE LWIR CAMERA - FLIR A655sc," (accessed Oct. 08, 2019). [Online]. Available: https://www.flir.com/products/a655sc/

[22] G. W. H. Höhne, W. F. Hemminger, and H.-J. Flammersheim, *Differential Scanning Calorimetry*. Springer, 2003.

[23] "DSC 2500 - Discovery DSC Series," (accessed Nov. 12, 2019). [Online]. Available: https://www.tainstruments.com/dsc-2500/

[24] M. Kostryukova, "Specific heat of Nickel-Zinc system ferrites in the low-temperature region," *Journal of Experimental and Theoretical Physics*, vol. 40, no. 6, pp. 1638–1643, 1961.

[25] N. W. Grimes, "On the specific heat of compounds with spinel structure," *Proc. of the Royal Society of London. Series A, Mathematical and Physical Sciences*, vol. 338, no. 1613, pp. 209–221, 1974.

[26] S. Ziemniak, L. Anovitz, R. Castelli, and W. Porter, "Magnetic contribution to heat capacity and entropy of nickel ferrite (NiFe2O4)," *Journal of Physics and Chemistry of Solids*, vol. 68, no. 1, pp. 10 – 21, 2007.

[27] "EPCOS Data Book 2013 - Ferrites and Accessories," (accessed Nov. 19, 2019). [Online]. Available: https://www.tdk-electronics.tdk.com/download/519704/069c210d0363d7b4682d9ff22c2ba503/ferrites-and-accessories-db-130501.pdf

[28] D. Neumayr, D. Bortis, J. W. Kolar, S. Hoffmann, and E. Hoene, "Origin and quantification of increased core loss in MnZn ferrite plates of a multi-gap inductor," *CPSS Transactions on Power Electronics and Applications*, vol. 4, no. 1, pp. 72–93, March 2019.

[29] "NTC Thermistors | Epoxy Type," (accessed May 27, 2020). [Online]. Available: https://amphenol-sensors.com/en/thermometrics/ntc-thermistors/epoxy/3334-type-65?highlight=WyJtYzY1Il0=

[30] "Keysight Technologies - 34410A and 34411A Multimeters," (accessed May 27, 2020). [Online]. Available: https://www.keysight.com/us/en/assets/7018-01326/data-sheets/5989-3738.pdf

[31] "SIFERRIT material N49," (accessed Jan. 07, 2020). [Online]. Available: https://www.tdk-electronics.tdk.com/download/528856/cf394eea3fae828c345f46dc297b76ab/pdf-n49.pdf

[32] V. Valchev and A. Van den Bossche, *Inductors and Transformers for Power Electronics*. CRC Press, 2005.

[33] T. Guillod, F. Krismer, and J. W. Kolar, "Magnetic equivalent circuit of MF transformers: modeling and parameter uncertainties," *Springer Nature, Electrical Engineering*, vol. 100, no. 4, pp. 2261–2275, Dec. 2018.

[34] "COMSOL Multiphysics® v. 5.4." (COMSOL AB, Stockholm, Sweden). [Online]. Available: www.comsol.com

[35] "Ferrite Magnetic Design Tool," (accessed Jan. 13, 2020). [Online]. Available: https://www.tdk-electronics.tdk.com/en/180490/design-support/design-tools/ferrite-magnetic-design-tool

[36] "67 Material Data Sheet," (accessed Dec. 19, 2019). [Online]. Available: https://www.fair-rite.com/67-material-data-sheet/

[37] M. Gopal, *Control Systems: Principles and Design*. McGraw-Hill Education, India, 2002.

[38] "HDO4054A," (accessed Aug. 12, 2020). [Online]. Available: https://teledynelecroy.com/oscilloscope/hdo4000a-high-definition-oscilloscopes/hdo4054a

[39] "Arbitrary Waveform Generators - WaveStation 2052," (accessed Jan. 07, 2020). [Online]. Available: https://teledynelecroy.com/wavestation/detail.aspx?modelid=6865&capid=131&mid=1043

[40] "150A100D," (accessed June 02, 2020). [Online]. Available: https://www.arworld.us/post/150A100D.pdf

[41] "Types MC and MCN Multilayer RF Capacitors," (accessed June 03, 2020). [Online]. Available: https://www.cde.com/resources/catalogs/MC.pdf

[42] J. de Lau, "Influence of chemical composition and microstructure on high-frequency properties of Ni-Zn-Co ferrites," *Ph.D. dissertation, Technische Hogeschool Eindhoven*, 1975.

[43] P. Papamanolis, T. Guillod, F. Krismer, and J. W. Kolar, "Transient calorimetric measurement of ferrite core losses," in *Proc. of the IEEE Applied Power Electronics Conf. and Expo. (APEC)*, March 2020.

[44] "R&S®BBA150 Broadband Amplifier," (accessed Jan. 07, 2020). [Online]. Available: https://www.rohde-schwarz.com/product/bba150-products_63492-35728.html?change_c=true

Panteleimon Papamanolis (S'17) studied electrical engineering at the National Technical University of Athens (NTUA), with majors in energy conversion and electric power systems. In 2014 he continued his MSc studies at ETH Zürich in Robotics, Systems and Control. Since November 2016 he is with the Power Electronic Systems Laboratory at ETH Zurich as a Ph.D. student, focusing on the modeling, optimization and measurement of magnetic components and on 3-phase AC/DC rectifier converters for EV charging applications.

Thomas Guillod (M'18) received the M.Sc. degree in electrical engineering and information technology in 2013 from ETH Zurich, Switzerland with a focus on power electronics, numerical analysis, and field theory. In 2013, he joined the Power Electronic Systems Laboratory at ETH Zurich as a Ph.D. student and, in 2018, as a postdoctoral researcher. His current research interests include medium-voltage converters, high-frequency magnetic components, design and optimization methods, and numerical modeling methods.

Florian Krismer (M'12) received the Dipl.-Ing. (M.Sc.) degree in electrical engineering with specialization in automation and control technology from the Vienna University of Technology, Vienna, Austria, in 2004, and the Ph.D. degree in electrical engineering from the Department of Information Technology and Electrical Engineering of ETH Zurich, Zurich, Switzerland, in 2010. He is currently a Research Associate at PES, where he has co-supervised Ph.D. students and has continued with his research in the field of power electronics. He is the author or coauthor of numerous conference and peer-review publications and has received two awards for his publications. His research interests include the analysis, design, and general optimization of power converter systems, e.g., the weight optimization of a bi-directional dc–dc converter for an airborne wind turbine. Furthermore, he conducts research related to the filtering of conducted electromagnetic emissions and collaborated in the littlebox-challenge with respect to the hardware realization.

Johann W. Kolar (F'10) received his M.Sc. degree in Industrial Electronics and Control Engineering and his Ph.D. degree in Electrical Engineering (summa cum laude/promotio sub auspiciis praesidentis rei publicae) from the Vienna University of Technology, Austria, in 1997 and 1999, respectively. Since 1984, he has been working as independent researcher and international consultant in close collaboration with the Vienna University of Technology, in the fields of power electronics, industrial electronics and high performance drive systems. He is currently a Full Professor and the Head of the Power Electronic Systems Laboratory at the Swiss Federal Institute of Technology (ETH) Zurich. He has proposed numerous novel PWM converter topologies, modulation and control concepts, multi-objective power electronics design procedures, etc. and has supervised 70+ Ph.D. students. He has published 900+ scientific papers in international journals and conference proceedings, 4 book chapters, and has filed 190+ patents. He has presented 30+ educational seminars at leading international conferences, has served as IEEE PELS Distinguished Lecturer from 2012 through 2016, and has received 36 IEEE Transactions and Conference Prize Paper Awards, the 2014 IEEE Power Electronics Society R. David Middlebrook Achievement Award, the 2016 IEEE William E. Newell Power Electronics Award, the 2016 IEEE PEMC Council Award, and two ETH Zurich Golden Owl Awards for excellence in teaching. He has initiated and/or is the founder of 4 ETH Spin-off companies. The focus of his current research is on ultra-compact and ultra-efficient SiC and GaN converter systems, ANN-based power electronics components and systems design, Solid-State Transformers, Power Supplies on Chip, as well as ultra-high speed and ultra-light weight drives, bearingless motors, and energy harvesting.